A detailed experimental and theoretical study of the femtosecond A-band photodissociation of CH3I

Rebeca de Nalda, Judith Durá, Alberto García-Vela, Jesús G. Izquierdo, Jesús González-Vázquez et al.

Additional information on J. Chem. Phys.

A detailed experimental and theoretical study of the femtosecond *A*-band photodissociation of CH$_3$I

Rebeca de Nalda,[1] Judith Durá,[2] Alberto García-Vela,[3] Jesús G. Izquierdo,[4]
Jesús González-Vázquez,[4,a)] and Luis Bañares[4,b)]

[1]*Instituto de Química Física Rocasolano, CSIC, C/ Serrano 119, 28006 Madrid, Spain*
[2]*Unidad Asociada Departamento de Química Física I, Facultad de Ciencias Químicas, Universidad Complutense de Madrid, 28040 Madrid, Spain*
and Instituto de Estructura de la Materia, CSIC, C/ Serrano 123, 28006 Madrid, Spain
[3]*Instituto de Física Fundamental, CSIC, C/ Serrano 123, 28006 Madrid, Spain*
[4]*Departamento de Química Física I, Facultad de Ciencias Químicas, Universidad Complutense de Madrid, 28040 Madrid, Spain*

The real time photodissociation dynamics of CH$_3$I from the *A* band has been studied experimentally and theoretically. Femtosecond pump-probe experiments in combination with velocity map imaging have been carried out to measure the reaction times (clocking) of the different (nonadiabatic) channels of this photodissociation reaction yielding ground and spin-orbit excited states of the I fragment and vibrationless and vibrationally excited (symmetric stretch and umbrella modes) CH$_3$ fragments. The measured reaction times have been rationalized by means of a wave packet calculation on the available *ab initio* potential energy surfaces for the system using a reduced dimensionality model. A 40 fs delay time has been found experimentally between the channels yielding vibrationless CH$_3(\nu=0)$ and I($^2P_{3/2}$) and I*($^2P_{1/2}$) that is well reproduced by the calculations. However, the observed reduction in delay time between the I and I* channels when the CH$_3$ fragment appears with one or two quanta of vibrational excitation in the umbrella mode is not well accounted for by the theoretical model. © *2008 American Institute of Physics.*
[DOI: 10.1063/1.2943198]

I. INTRODUCTION

Breaking and forming of chemical bonds and energy flow in molecules are at the very heart of chemistry. The experimental observation of chemical transformations in real time is the focus of femtochemistry, which utilizes ultrashort laser pulses to diagnose the time evolution of a chemical reaction. Two decades after the birth of this new field in chemistry[1,2] and with a wealth of accumulated information concerning molecular dynamics[3–9] even in very complex, often biologically relevant systems,[3,10–14] basic questions about the real time dynamics of simple systems still remain to be explored. It is only via the combination of recently developed detection techniques and the full exploitation of state-of-the-art femtosecond laser systems that we can hope to address them.

Since the conception of femtochemistry, a large variety of detection techniques have been employed to probe ultrafast reaction dynamics,[2,3] including laser induced fluorescence, photoelectron spectroscopy, and time-of-flight mass spectrometry, among others. Multiphoton ionization is used in many laboratories along with time-of-flight mass spectrometry for two main reasons: mass resolution allows the identification of reaction species and intermediates, and the

detection of ions is very efficient. However, three major problems have typically hampered in the past the realization and interpretation of femtosecond experiments in reaction dynamics when measuring ions: (1) the numerous competing multiphoton channels that inevitably open up under intense femtosecond laser irradiation, including dissociative ionization, (2) the typically low yield of the (neutral) channels under study, consequence of the former, and (3) the difficulties to achieve tunability with most femtosecond laser systems, which makes difficult, in general, the use of resonant detection schemes.

Zewail and co-workers carried out femtosecond pump-probe experiments in combination with kinetic energy time-of-flight mass spectrometry[15] using resonant multiphoton ionization of the product fragments. In these experiments, they were able to exploit the temporal, velocity, angular, and state dynamics to study a large variety of uni- and bimolecular reactions in real time.[4] Using this technique, the dynamics of transition states and final products can be observed at the same time by varying the delay time between the pump and probe laser pulses and using only one wavelength for the probe and resolving the kinetic energy. This approach is similar to the anion femtosecond photoelectron spectroscopy introduced by Greenblatt *et al.*,[16] in which a femtosecond laser pulse is used to excite a ground-state anion to a repulsive excited state, and a second femtosecond laser pulse is then used to detach the electron from the anion. When the wave packet is mapped onto the accessible neutral surfaces,

the evolution of the resulting different kinetic energy electrons directly reflects the dissociation dynamics of the anion. More recently, velocity map imaging[17,18] used in combination with pump-probe femtosecond laser pulses has demonstrated to be a powerful technique to study the real time dynamics of complex systems.[3,8,19–21] Femtosecond imaging experiments include photoelectron[3,22] and photoion-photoelectron coincidence detection.[3,6,7,22]

Here we have studied the femtosecond photodissociation dynamics of CH_3I from the A band both experimentally and theoretically. Experimentally, the velocity map imaging technique, which provides selectivity at the detection end, has been combined with tunable UV femtosecond laser radiation, which provides selectivity and resonant enhancement at the probe end by resonance enhanced multiphoton ionization (REMPI) of the products. From a theoretical viewpoint, wave packet calculations have been carried out on the available *ab initio* potential energy surfaces using a reduced dimensionality model.

Methyl iodide has been taken as a prototype for photodissociation studies of polyatomic molecules over the years. This molecule presents a relatively low number of atoms and an apparently simple dissociation process. For this reason, it has been considered as a benchmark where experimental and theoretical techniques have been tested for more than two decades. There exists a vast literature on the photodissociation of CH_3I that traces back to the discovery of the first chemical laser by Kasper and Pimentel, emitting radiation at 1.3 μm that corresponds to the I atom $^2P_{3/2} \leftarrow {}^2P_{1/2}$ transition.[23] For a selection of papers on the photodissociation of CH_3I, see, for instance, Refs. 24–37. Most of the studies have focused on the near UV photodissociation dynamics via excitation in the first absorption band (A band), a broad featureless absorption continuum (220–350 nm) with a maximum at about 260 nm. It is well known that the lowest energy electronic excitation in CH_3I corresponds to a $n \rightarrow \sigma^*$ transition, where a nonbonding p electron of iodine is promoted to the lowest energy available antibonding molecular orbital. As a consequence of the strong spin-orbit coupling the electronic configuration gives rise to five states: E, E, A_1, A_2, and E for $\Omega = 2, 1, 0^+, 0^-$, and 1, respectively.[38] In Mulliken notation,[39] these five states are denoted as $^3Q_2$, $^3Q_1$, $^3Q_{0^+}$, $^3Q_{0^-}$, and $^1Q_1$. Only the $^3Q_{0^+}$ state correlates with the $CH_3(\tilde{X}\,^2A_2'') + I^*(^2P_{1/2})$ products, while the rest of the excited states correlate with $CH_3(\tilde{X}\,^2A_2'') + I(^2P_{3/2})$. Thus, a curve crossing must exist between the $^1Q_1$ and $^3Q_{0^+}$ states and this crossing complicates the origin of the $I(^2P_{3/2})$ fragments, since, in principle, they can be produced both adiabatically and nonadiabatically. Three of the five states assigned by Mulliken are accessible through dipole allowed transitions: two weak perpendicular transitions to the $^3Q_1$ and $^1Q_1$ states and a strong parallel transition to the $^3Q_{0^+}$ state (in what follows the $^3Q_{0^+}$ state will be denoted $^3Q_0$). The concerted theoretical and experimental efforts have unraveled that most of the absorption can be attributed to the $^3Q_0$ state, and the $I(^2P_{3/2})$ fragment observed in the experi-
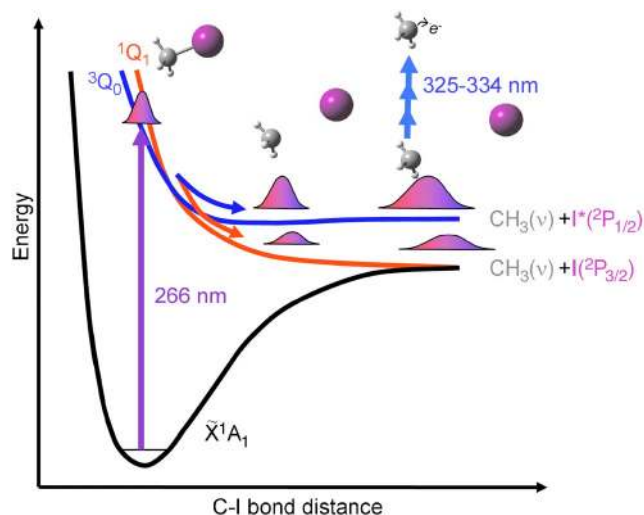

FIG. 1. (Color online) Schematic graph of the relevant potential energy curves along the C–I bond representing A-band photodissociation of CH_3I. A nuclear wave packet on the $^3Q_0$ potential energy curve is produced by the pump (266 nm) femtosecond laser pulse. The larger part of the wave packet evolves adiabatically along the $^3Q_0$ surface correlating to $CH_3 + I^*(^2P_{1/2})$, but a section of it leaks nonadiabatically to the $^1Q_1$ surface correlating to $CH_3 + I(^2P_{3/2})$. The different products are probed by a time-delayed femtosecond laser pulse that induces a $2+1$ REMPI process of the CH_3 fragment.

ments is then the result of a nonadiabatic transition at the conical intersection between the $^3Q_0$ and $^1Q_1$ states (see Fig. 1).

The most salient features of the photodissociation of CH_3I from the A band evidenced experimentally (see Ref. 34 for a review) suggest that about 90% of the available energy appears as fragments' kinetic energy, although a substantial vibrational excitation on the umbrella mode (ν_2) of CH_3 has been observed. In particular, the dissociation channel yielding $I(^2P_{3/2})$ show vibrational population inversion, in contrast with that in which $I^*(^2P_{1/2})$ is produced, where the most populated vibrational state is $\nu = 0$. Some experiments have also shown some vibrational excitation on the CH_3 symmetric stretch mode (ν_1). Rotational excitation of the CH_3 fragment is also larger for the $I(^2P_{3/2})$ channel, whereas in the channel yielding $I^*(^2P_{1/2})$, CH_3 appears rotationally colder. Another ingredient is the observed strong rotational alignment of the methyl radical. In general terms, the accepted dissociation mechanism for CH_3I in the A band is that of a direct, prompt bond breakage, in which a nonadiabatic crossing between surfaces is involved.

The first theoretical studies on the photodissociation of CH_3I were based on the model of Shapiro and Bersohn.[40] In this model, the dissociation reaction happens in linear configurations and the umbrella motion of the CH_3 fragment is treated as a C–X stretch mode, where X is a hypothetical atom located in the center of mass (CM) of the H_3. In the first studies, empirical potential surfaces that were built to agree with the measured absorption spectrum and vibrational distributions of the CH_3 fragment were used. Later models[41,42] used two diabatic potential surfaces and a radial nonadiabatic coupling term to reproduce the two observed dissociation channels. A significant advance on the theoretical understanding of the CH_3I system came with the *ab initio*

calculations by Amatatsu *et al.* and the construction of the corresponding potential energy surfaces for the two states ($^3Q_0$ and $^1Q_1$) involved in the photodissociation, first in six dimensions[43] and later in full nine dimensions.[32] These potential surfaces were used in classical trajectory[32,43] and wave packet calculations.[31,44,45] Improved potential energy surfaces were produced by Xie *et al.*[35] based on contracted spin-orbit configuration interaction calculations using a larger basis set and more spin-free configurations, in order to better reproduce the absorption spectrum of CH$_3$I. These improved potential surfaces were used in reduced dimensionality wave packet calculations of rotational state selected CH$_3$I and CD$_3$I.[35] All calculations up to now have focused only on asymptotic properties (product fragment state distributions) and have compared well with the existing experimental data. New *ab initio* calculations have been carried out more recently[46,47] with the main aim of improving the agreement between the experimental and calculated absorption spectrum of CH$_3$I.[48]

The photodissociation of CH$_3$I was the first system to be studied by ion imaging,[26] and more recently, comprehensive velocity map imaging experiments of the *A* band photodissociation of CH$_3$I have been carried out with nanosecond lasers.[33,34] It is the existence of the nonadiabatic crossing between the $^3Q_0$ and $^1Q_1$ states and the possibility of probing different vibrational states of the methyl fragment that makes the *A* band photodissociation of CH$_3$I an ideal system for real time studies. However, experiments using femtosecond laser pulses have been scarce and mostly concerned with photodissociation of Rydberg states.[49,50] Zhong and Zewail[4] were able to clock the reaction time in the *A* band photodissociation of CH$_3$I by using the gated time-resolved KETOF mass spectrometry technique. In these experiments, resonant detection of both I($^2P_{3/2}$) and I*($^2P_{1/2}$) fragments was carried out and a global reaction time of 125 fs was obtained. However, these experiments did not have enough resolution to distinguish between the two main dissociation channels yielding I($^2P_{3/2}$) and I*($^2P_{1/2}$) or to obtain data on channels where the CH$_3$ fragment appears with different degrees of vibrational excitation.

In a previous report from our group,[51] the real time multichannel photodissociation dynamics of CH$_3$I from the *A* band were studied using femtosecond pump-probe and velocity map imaging techniques and resonant multiphoton ionization of vibrationless CH$_3$ fragments. In that work, it was possible to clock the C–I bond rupture of CH$_3$I from the *A* band, which involves nonadiabatic dynamics yielding ground-state I($^2P_{3/2}$) and spin-orbit excited I*($^2P_{1/2}$) and ground and vibrationally excited CH$_3$ fragments. In particular, a delay of about 40 fs was found between the channels yielding ground vibrational state CH$_3$($\nu=0$) and I($^2P_{3/2}$) and I*($^2P_{1/2}$).

In the present work, we present an extension of the previous study, containing new results on the influence of the fragment vibrational energy content and off-resonant measurements. We initiate the reaction by a femtosecond pump pulse at 266 nm as sketched in Fig. 1. Once the wave packet is formed in the $^3Q_0$ potential surface, the dynamics are probed by a time-delayed femtosecond pulse centered at

333.5, 329.4, or 325.8 nm, which ionizes ground-state CH$_3$ fragments by 2+1 resonance enhanced multiphoton ionization on the Q branch of the $3p_z$ $^2A_2'' \leftarrow ^2A_2''$ 0_0^0, 2_1^1, or 2_2^2 transitions, respectively. The broadband nature of the femtosecond probe pulse gives us the possibility of also probing CH$_3$ fragments with one quantum of vibrational excitation in the ν_1 stretching mode (1_1^1 transition). Thus, we record the appearance of different vibrational states of CH$_3$ together with I($^2P_{3/2}$) or I*($^2P_{1/2}$). Additionally, a wave packet calculation has been performed using a pseudotriatomic model for the system, focusing on time-resolved properties, in order to rationalize the experimental observations. The paper is organized as follows: Secs. II and III briefly describe the experimental setup and theoretical approach. Sections IV and V present the most relevant experimental and theoretical results. In Sec. VI both experimental and theoretical results are discussed and the paper closes in Sec. VII with the main conclusions.

II. EXPERIMENT

The experimental setup is shown schematically in Fig. 2. The laser is a Spectra-Physics amplified Ti:sapphire system delivering 80 fs, 1 mJ pulses centered at 800 nm with 1 kHz repetition rate. The fundamental output is split into two arms in a 80:20 beam splitter. The weaker 0.2 mJ beam is frequency tripled in a third harmonic generation unit and provides the 266 nm pump beam for the experiment. The remaining 0.8 mJ beam is used to pump an optical parametric amplifier (OPA), where signal and idler pulses are generated in a BBO crystal with wavelengths around 1.3 and 2 μm, respectively. The signal pulse is later frequency quadrupled to constitute the probe beam around 325–334 nm. A computer-controlled, motorized delay stage in the pump arm provides controllable delay between the two pulses with around 0.3 fs precision. Beam energies are around 1 and 3 μJ/pulse for the pump and probe beams, respectively. The time duration of the pump and probe pulses is estimated to be around 100 fs, limited by the observed cross correlation of $\approx$200 fs. The bandwidth of both pump and probe lasers is $\approx$3 nm full width at half maximum (FWHM). Independent polarization control in each arm is provided by the use of half-wave plates, and telescopes are used to control their focusing geometry on target. The pump and probe laser beams are propagated into the vacuum chamber collinearly and focused with a 25 cm focal length lens into the interaction region of the chamber. Their polarization is kept parallel to the detector face to provide the cylindrical symmetry required for the procedure of Abel inversion of the ion images (see below).

The vacuum chamber is divided into three sections: source, ionization, and detection. The molecular beam is generated in the source chamber; this chamber is differentially pumped from the other two. In it, a supersonic molecular pulsed beam of 10% CH$_3$I seeded in He (1.5 bars) is formed in a 1 kHz piezoelectric home-made valve.[52] During the experiments, the CH$_3$I sample is kept in ice to reduce the vapor pressure and thus cluster formation. With that same aim, the lasers are fired in the early part of the molecular
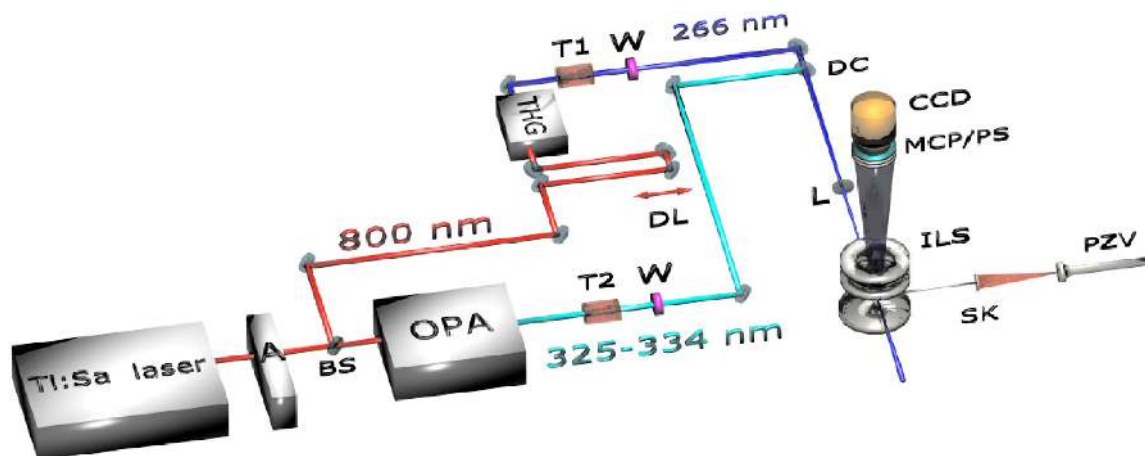
FIG. 2. (Color online) Schematic representation of the experimental setup. A Ti:sapphire amplified laser system (1 mJ, 80 fs, 1 kHz) is split into two arms that provide the frequency-tripled pump beam (266 nm) and the tunable probe beam [325–334 nm, output of an optical parametric amplifier, (OPA)]. (BS) beam splitter, (A) autocorrelator, (W) half-wave plate, (T1) and (T2) telescopes, (L) lens, (DC) dichroic mirror, (DL) delay line, (PZV) 1 kHz piezoelectric valve, (SK) skimmer, (ILS) ion lens system, (MCP) microchannel plates, (PS) phosphor screen, and (CCD) charge-coupled device camera. Copropagating pump and probe femtosecond pulses are focused in the CH_3I/He molecular beam. The 3D distribution of a given fragment ion is extracted, accelerated, and projected on an imaging detector consisting of a MCP/PS coupled to a CCD camera, where the velocity map images are recorded as a function of pump-probe delay time.

beam pulse. The molecular beam passes through a 0.5 mm skimmer that separates the source chamber from the ionization chamber. Once in the ionization chamber, the molecular beam flies between the repeller and the extractor plates of a gridless ion lens electrode system, where it is intersected perpendicularly by the laser beams. The ions created in the interaction region are extracted perpendicularly towards a 60 cm time-of-flight tube at the end of which sits the detector, a dual microchannel plate (MCP) in Chevron configuration coupled to a phosphor screen. Appropriate voltages to the electrodes are applied so that velocity mapping configuration[17] is achieved, i.e., all ions with the same kinetic energy are mapped on the same point on the plane of the detector. Optimum velocity mapping conditions were obtained with $V_{extractor}/V_{repeller}=0.785$ ($V_{repeller}=5200$ V). By applying a gated voltage to the front plate of the MCP, its gain is gated, so that a selective detection of ion masses can be achieved. The two-dimensional (2D) mass-selected ion images on the phosphor screen are recorded with a Peltier-cooled 12-bit CCD camera and stored in a computer. The velocity, and thus the kinetic energy, of the ions, was calibrated using methyl images produced in the photodissociation of CH_3I for a long time delay between the pump and probe pulses, using the known kinetic energy release of the $CH_3(\nu=0)+I^*(^2P_{1/2})$ and $CH_3(\nu=0)+I(^2P_{3/2})$ channels. In these conditions, the kinetic energy resolution of the apparatus is better than 100 meV at 1 eV kinetic energy release.

The methodology in a typical experiment is as follows: cold CH_3I molecules are excited into the dissociative *A* band by the 266 nm pump beam. After a varying delay in the range of tens or hundreds of femtoseconds, the resulting neutral fragments, in particular CH_3, are ionized in a 2+1 REMPI process by the probe beam. Tunability of the probe laser, to cover several vibronic transitions in CH_3, is achieved by adjusting the phase matching angle of the parametric BBO crystal of the optical parametric amplifier. The ions resulting from the process are mass selected and imaged

onto the detector and accumulated for an exposure time that could be varied in the range of $0.1-10^5$ ms. A typical time delay scan is a sweep of 2000–5000 fs in steps of 20–50 fs, with the acquisition of one ion image per delay point. The image is the result of accumulating over 10–60 s, i.e., it corresponds to the accumulation of some tens of thousands of laser shots. The acquisition and storage process, together with the control of the position of the delay line, is fully computer automatized.

The raw images are Abel inverted with the pBasex method,[53] where polar coordinates are applied for the inversion. This way, the noise produced in the mathematical procedure is concentrated in the middle of the image instead of a vertical axis, allowing a cleaner analysis of the images in the regions of interest. Time zero, defined as the position of temporal overlap between the pump and probe lasers on target, and also their cross-correlation function, are given by the *in situ* measurement of the parent ion transient of N,N-diethyl aniline by 1+1′ REMPI.

III. THEORETICAL MODEL

A. Model system

The methyl iodide system is represented by means of the reduced dimensionality model of Guo.[44,54] This model considers the CH_3I system as a CXI pseudotriatomic molecule where the pseudoatom X (X=H_3) is located at the CM of the three H atoms. In the model, three degrees of freedom represented by the (R,r,θ) Jacobi coordinates are included, where the dissociation coordinate R is the distance between I and the CH_3 (or C-X) CM, r is the C-X distance and it represents the umbrella bend of the C–H_3 group (ν_2), and θ is the angle between the vectors associated with R and r and it represents the X-C-I bend (ν_6). The assumption of modeling the umbrella mode of the C–H_3 group in CH_3I as a C-X stretch has been justified by a number of theoretical works, including both three[35,44,45,54] and two[40–42,55] dynamical de-

grees of freedom, which were successful in reproducing most of the experimental data. The good performance of the model relies on the fact that dissociation occurs mainly along collinear configurations.

In the simulations zero total angular momentum, $J=0$, is assumed for the system, and then the nuclear kinetic energy operator can be expressed as

$$\hat{T} = -\frac{\hbar^2}{2\mu}\frac{\partial^2}{\partial R^2} - \frac{\hbar^2}{2m}\frac{\partial^2}{\partial r^2} + \left(\frac{1}{2\mu R^2} + \frac{1}{2I_{CH_3}}\right)\hat{j}^2, \quad (1)$$

where the reduced masses for CH_3I are defined as

$$\mu = \frac{m_I(m_C + m_{H_3})}{m_I + m_C + m_{H_3}}, \quad m = \frac{m_C m_{H_3}}{m_C + m_{H_3}}. \quad (2)$$

In the present model the moment of inertia I_{CH_3} is assumed to be only the perpendicular component of the total moment of inertia,[44,56]

$$I_{CH_3} = m_H r_e^2 (1 - \cos\gamma) + \frac{m_H m_C}{3m_H + m_C} r_e^2 (1 + 2\cos\gamma), \quad (3)$$

being the H-C-H angle γ related to r through the relationship

$$\cos\gamma = 1.0 - 1.5\left[1.0 - \left(\frac{r}{r_e}\right)^2\right], \quad (4)$$

where it is assumed that the C_{3v} symmetry is preserved for CH_3. The C-H distance r_e has been fixed in our simulations to the value $r_e = 2.065\,73a_0$ in the case of the ground electronic state of the system, and to the value $r_e = 2.052\,66a_0$ in the case of the $^3Q_0$ and $^1Q_1$ excited electronic states. The value $r_e = 2.065\,73a_0$ corresponds to the C-H distance in the equilibrium geometry of the ground state of CH_3I with C_{3v} symmetry found by *ab initio* calculations,[32] while $r_e = 2.052\,66a_0$ is the C-H distance found by the same calculations for the CH_3 equilibrium geometry with D_{3h} symmetry at very large CH_3-I separations.

B. Potential energy surfaces and initial state

Photodissociation of CH_3I in the A band takes place upon excitation of the system from the $\tilde{X}\,^1A_1$ ground electronic state to the $^3Q_0$ excited electronic state [correlating with the $CH_3+I^*(^2P_{1/2})$ products], which in turn is nonadiabatically coupled to the $^1Q_1$ excited state [correlating with the $CH_3+I(^2P_{3/2})$ products]. Thus, at least three electronic potential energy surfaces are involved in the photolysis process. The $\tilde{X}\,^1A_1$ ground electronic potential surface is represented as a sum of three potential interactions

$$V_g(R_{C-I}, r, \theta) = V_a(R_{C-I}) + V_b(r) + V_c(\theta), \quad (5)$$

where the $V_a(R_{C-I})$ interaction in the R_{C-I} coordinate is taken from the CH_3I 2D ground-state potential recently reported by Alekseyev *et al.* and computed through multireference spin-orbit configuration interaction *ab initio* calculations.[47] In this *ab initio* potential the C-I equilibrium distance is $R_{C-I} = 4.04a_0$, and the calculated values of $D_e(CH_3-I)$ and $D_0(CH_3-I)$ are 2.432 and 2.26 eV, respectively, this latter quantity deviating ~0.15 eV from the experimental value $D_0(CH_3-I) = 2.41 \pm 0.02$ eV.[34] Since the R_{C-I} coordinate

does not coincide with the Jacobi coordinate R used in the calculations, the $V_a(R_{C-I})$ potential in Eq. (5) is transformed to the (R, r, θ) coordinates in order to obtain a ground potential surface $V_g(R, r, \theta)$.

The $V_b(r)$ and $V_c(\theta)$ interactions are represented by harmonic oscillator functions

$$V_b(r) = \tfrac{1}{2}k_b(r - r_0)^2, \quad V_c(\theta) = \tfrac{1}{2}k_c\theta^2. \quad (6)$$

In the case of $V_b(r)$ the force constant is $k_b = m\omega_b^2$, with $\omega_b = 1254$ cm^{-1} and $r_0 = 0.6555a_0$. For the $V_c(\theta)$ potential $k_c = \mu_c\omega_c^2$, with $\omega_c = 883$ cm^{-1} and the bending reduced mass μ_c being given by[44]

$$\frac{1}{\mu_c} = \frac{1}{m_I r_{C-I}^2} + \frac{1}{m_{H_3} r_{C-H_3}^2} + \frac{1}{m_C}\left(\frac{1}{r_{C-I}^2} + \frac{1}{r_{C-H_3}^2} + \frac{2}{r_{C-I}r_{C-H_3}}\right), \quad (7)$$

which by replacing the different distances and masses by their proper values gives the quantity $\mu_c = 1767.784$ amu.

Regarding the excited electronic states $^3Q_0$, $^1Q_1$, and the nonadiabatic coupling between them, in the simulations we have used the *ab initio* surfaces calculated by Xie *et al.*,[35] which are an improved version of the previous nine-dimensional surfaces of Amatatsu *et al.*[32] The surfaces and nonadiabatic couplings of Refs. 35 and 32 have the same functional form, only differing in the value of some of the parameters used to fit the *ab initio* points. Since the surfaces and couplings between them have been described in detail in Ref. 32, in the following we shall use the notation of that work when we refer to them. Specifically, we have used the diabatic potential surfaces V_1 and V_3 in the notation of Ref. 32, which correspond to the $^1Q_1(A')$ and $^3Q_0(A')$ electronic states, respectively, nonadiabatically coupled by the V_{13} coupling. The three surfaces V_1, V_3, and V_{13} are nine-dimensional ones, and in order to reduce their dimensionality, six out of the nine coordinates have been fixed at their equilibrium values. To this purpose the three C-H distances are fixed to the value $r_1 = r_2 = r_3 = 2.052\,66a_0$. In addition, the angle ϕ between the plane containing the I-C bond and the plane containing one of the C-H bonds is fixed to 0°, and the three β angles (one of which is redundant) between the two planes containing C-H bonds are fixed to $\beta_1 = \beta_2 = \beta_3 = 120°$ (see Fig. 1 of Ref. 32). The resulting three-dimensional (3D) surfaces are transformed to the (R, r, θ) Jacobi coordinates employed in the simulations.

The initial state of CH_3I is calculated variationally on the ground electronic potential surface $V_g(R, r, \theta)$ by solving the Schrödinger equation

$$[\hat{T} + V_g(R, r, \theta)]\psi(R, r, \theta) = E\psi(R, r, \theta), \quad (8)$$

where $\hat{T}$ is expressed as in Eq. (1). A rigorous variational solution of Eq. (8) involves diagonalization of an extremely large Hamiltonian matrix, which becomes impractical. Thus, in order to make the problem tractable an adiabatic approximation was applied. In a first step the Schrödinger equation

$$\left[-\frac{\hbar^2}{2m}\frac{\partial^2}{\partial r^2} + \left(\frac{1}{2\mu R^2} + \frac{1}{2I_{CH_3}}\right)\hat{j}^2 + V_g(R,r,\theta)\right]\varphi(R;r,\theta)$$
$$= \varepsilon(R)\varphi(R;r,\theta) \tag{9}$$

is solved for fixed values of the R coordinate in a uniform grid of 401 equidistant points in the range $3.5a_0 \leqslant R \leqslant 16.0313a_0$ with a step $\Delta R = 0.0313a_0$. Solution of Eq. (9) for each fixed R distance is obtained by representing the Hamiltonian matrix in a basis set in the r and θ coordinates and diagonalizing. The Fourier grid Hamiltonian (FGH) method[57] was used to represent the radial coordinate r in a grid of 33 equidistant points in the range $-1.6a_0 \leqslant r \leqslant 1.703a_0$, while a basis of 24 Legendre polynomials was used to represent the angular coordinate θ.

After solving Eq. (9) the functions $\varphi(R;r,\theta)$ and $\varepsilon(R)$ are obtained. Now, using $\varepsilon(R)$ as a potential energy function we solve the equation

$$\left[-\frac{\hbar^2}{2\mu}\frac{\partial^2}{\partial R^2} + \varepsilon(R)\right]\chi(R) = E\chi(R), \tag{10}$$

using again the FGH method. The initial state of CH_3I is the ground vibrational state of the system obtained as outlined above, which is represented as

$$\psi(R,r,\theta) = \chi(R)\varphi(R_e;r,\theta), \tag{11}$$

where R_e is the R equilibrium distance in the ground electronic potential surface. The energy associated with this initial state is $E = -18\,736.44$ cm^{-1}, relative to the asymptote of the ground potential surface which is located at the zero of energy.

C. Wave packet simulations

In the simulations it is assumed that CH_3I is excited from the $\widetilde{X}\,^1A_1$ state only to the $^3Q_0$ excited electronic state. The electric-dipole moment function $\mu_{ge}(R_{C-I})$ for this parallel $^3Q_0 \leftarrow \widetilde{X}\,^1A_1$ transition has been taken from the recent *ab initio* calculations of Alekseyev *et al.*[48] This *ab initio* function was calculated in the range $R_{C-I} = (3.8-4.75)a_0$, where it has the form of a nearly straight line, reaching the value $\sim$1 D around $R_{C-I} = 4.75a_0$. Thus we have fitted a straight line $\mu_{ge}(R_{C-I}) = aR_{C-I} - b$ to the *ab initio* values, with $a = 0.59$ and $b = 1.92$, in the R_{C-I} range where $\mu_{ge}(R_{C-I}) \leqslant 1$ D, and this function is transformed to the (R,r,θ) Jacobi coordinates. For larger distances of the Jacobi R coordinate the transition moment function $1/\{1+\exp[2(R-9.8)]\}$ suggested by Shapiro[41] has been used.

The time-dependent pump-probe experiments to be simulated use laser pulses of finite time duration, in the femtosecond regime. This aspect has been taken into account in the simulations by modeling the $^3Q_0 \leftarrow \widetilde{X}\,^1A_1$ excitation of CH_3I by means of a pump laser pulse which is assumed to have a Gaussian profile

$$A(t) = Ae^{-(t-t_0)^2/2\sigma^2}, \tag{12}$$

where $A = 0.001$, $t_0 = 0$ fs, and $\sigma = 42.5$ fs. This pulse extends over a temporal range of 300 fs (from $t = -150$ to $t = 150$ fs) and has a FWHM of 100 fs, which is approximately the

width estimated for the pump laser pulses produced in the experiments. By pumping the system initial state with such a pulse, a wave train is created in the $^3Q_0$ excited state along time which will evolve towards dissociation.

For the sake of simplicity, in the following we shall denote the three electronic states $\widetilde{X}\,^1A_1$, $^3Q_0$, and $^1Q_1$ involved in the photodissociation process by $|0\rangle$, $|1\rangle$, and $|2\rangle$, respectively, and correspondingly, their associated potential surfaces by $\hat{V}_0$, $\hat{V}_1$, and $\hat{V}_2$. The nonadiabatic coupling between the excited states $|1\rangle$ and $|2\rangle$ will be denoted by $\hat{V}_{12}$. The states $|0\rangle$ and $|1\rangle$ are radiatively coupled by the transition dipole moment and the radiation electric field through the coupling $\mu_{01}E(t)$, where μ_{01} is the $^3Q_0 \leftarrow \widetilde{X}\,^1A_1$ transition moment function described above, and the (linearly polarized) electric field has the form $E(t) = A(t)\cos\omega_0 t$. The frequency ω_0 is the photon frequency of the incident radiation, which in our case corresponds to the wavelength $\lambda = 266$ nm.

The wave packet can be expressed as

$$\Phi(R,r,\theta,\mathbf{Q},t) = \psi_0(R,r,\theta,t)|0\rangle + \psi_1(R,r,\theta,t)|1\rangle$$
$$+ \psi_2(R,r,\theta,t)|2\rangle, \tag{13}$$

with $\mathbf{Q}$ denoting the electronic coordinates. The time evolution of the amplitudes ψ_0, ψ_1, and ψ_2 on the three electronic potential-energy surfaces is governed by the following time-dependent coupled equations:

$$i\hbar\frac{\partial\psi_0}{\partial t} = \hat{H}_0\psi_0 - \mu_{01}A(t)\cos\omega_0 t\psi_1,$$

$$i\hbar\frac{\partial\psi_1}{\partial t} = \hat{H}_1\psi_1 - \mu_{10}A(t)\cos\omega_0 t\psi_0 + \hat{V}_{12}\psi_2,$$

$$i\hbar\frac{\partial\psi_2}{\partial t} = \hat{H}_2\psi_2 + \hat{V}_{21}\psi_1, \tag{14}$$

where $\hat{H}_i = \hat{T}_i + \hat{V}_i$ [$\hat{T}_i$ being expressed as in Eq. (1)], $\mu_{10} = \mu_{01}$, and $\hat{V}_{21} = \hat{V}_{12}$. Solution of Eq. (14) is subject to the initial condition $\psi_0(R,r,\theta,t=0) = \psi(R,r,\theta)$, $\psi_1(R,r,\theta,t=0) = \psi_2(R,r,\theta,t=0) = 0$.

In order to solve Eq. (14) the wave packet is represented in a basis set consisting of a two-dimensional rectangular grid for the radial coordinates and an angular basis including 24 Legendre polynomials for the θ coordinate. The rectangular grid consists of 400 equidistant points in the R coordinate in the range $3.5a_0 \leqslant R \leqslant 16.0a_0$ and 32 equidistant points in the r coordinate distributed in the range $-1.6a_0 \leqslant r \leqslant 1.6a_0$. The wave packet is propagated using the Chebychev polynomial expansion method[58] to express the evolution operator. Propagation was carried out for 450 fs with a time step $\Delta t = 0.1$ fs. The wave packet is absorbed at the edge of the grid in the R coordinate after each propagation time step by multiplying each ψ_i packet by the function $\exp[-\alpha(R-R_{abs})^2]$, with $\alpha = 0.9a_0^{-2}$ and $R_{abs} = 13.0a_0$.

D. Calculation of observable magnitudes

Dissociation of CH$_3$I occurs through two fragmentation channels, namely, CH$_3$+I* and CH$_3$+I, where the CH$_3$ fragment is produced with a distribution of internal states. Analysis of the population of such internal states provides valuable information on the CH$_3$I photodissociation process, and it has been the main goal of the simulations. In our theoretical model CH$_3$ is treated as a C-X pseudodiatomic molecule, which implies that only two internal degrees of freedom are considered, namely, the C-X stretch vibration (which approximates the CH$_3$ umbrella mode) and the C-X rotation. The eigenstates associated with these internal modes of the C-X fragment are represented by the product $\chi_\nu^{(j)}(r)P_j(\cos\theta)$, where $P_j(\cos\theta)$ is a normalized Legendre polynomial and $\chi_\nu^{(j)}(r)$ are the solutions of the equation

$$\left[-\frac{\hbar^2}{2m}\frac{\partial^2}{\partial r^2}+\frac{j(j+1)\hbar^2}{2I_{CH_3}}+V_{CH_3}(r)\right]\chi_\nu^{(j)}(r)=E_{\nu,j}\chi_\nu^{(j)}(r),$$

(15)

where $V_{CH_3}(r)$ is the CH$_3$ (or C-X) interaction potential at very large separation from the I atom,[32] and $E_{\nu,j}$ are the energies associated with the eigenstates.

Population of the CH$_3$ internal states is computed as a function of time by projecting out the wave packet onto the corresponding states. These populations are obtained by means of the method of Balint-Kurti *et al.*,[59,60]

$$P_{\nu,j}^{(i)}(E,t)=C\nu_0 k_{\nu,j}^{(i)}\left|\int_0^t\langle\chi_\nu^{(j)}(r)\right.$$

$$\left.\times P_j(\cos\theta)|\psi_i(R_c,r,\theta,t')\rangle e^{iEt'/\hbar}dt'\right|^2,$$

(16)

where C is a constant factor, $\nu_0=\omega_0/2\pi$ is the incident photon frequency (corresponding to $\lambda=266$ nm), $i=1,2$, R_c is a suitably large distance of the dissociation coordinate R, E is the total energy of the system reached with $\lambda=266$ nm radiation, $E=E_i+\hbar\omega_0$ (E_i being the energy of the CH$_3$I initial state), and $k_{\nu,j}^{(i)}$ is given by

$$k_{\nu,j}^{(i)}=[2m(E-\epsilon\delta_{i1}-E_{\nu,j})]^{1/2},$$

(17)

ϵ being the spin-orbit splitting between the two electronic states of I and δ_{i1} the Kronecker delta. The population in each vibrational state of the CH$_3$ umbrella mode can be calculated as

$$P_\nu^{(i)}(E,t)=\sum_j P_{\nu,j}^{(i)}(E,t).$$

(18)

IV. EXPERIMENTAL RESULTS

We have divided the experimental results in three sections. The first two sections will show resonant multiphoton ionization of the methyl fragment formed upon *A*-band photodissociation of CH$_3$I at 266 nm, the first concentrating on the formation of vibrationless methyl and the second, on umbrella mode excited methyl. We will show how the measure-

ments also show stretch mode excited methyl. The third section will briefly present results obtained upon detuning the probe laser from resonance.

A. Results on vibrationless CH$_3(\nu=0)$

In this and the next section, we present results on resonant multiphoton ionization of the methyl fragment resulting from the *A*-band photodissociation of CH$_3$I at 266 nm. Figure 3 shows a series of six Abel-inverted images corresponding to the CH$_3^+$ fragment measured for different pump-probe delay times for a probe laser wavelength centered at 333.5 nm [*Q* branch of the $3p_z(^2A_2''\leftarrow{}^2A_2'')$ 0_0^0 transition for a two-photon process]. The first image, taken at -300 fs, corresponds to the situation where the probe beam precedes the pump temporally. It shows a nonstructured contribution in the center of the image (i.e., low kinetic energy), which we attribute to a combination of multiphoton ionization processes induced by the pump and probe pulses. Later images witness the appearance of rings—channels with a well-defined kinetic energy—that are clearest for the later delay times. For a time delay of 1000 fs, we can consider that the dissociation process has taken place fully before the probe beam arrives, a situation that will be labeled as "asymptotic." Three rings can be observed in the images. The inner (stronger) and outer rings correspond to vibrationless CH$_3(\nu=0)$ formed in correlation with I*$(^2P_{1/2})$ and I$(^2P_{3/2})$, respectively. A third, weaker ring, can be seen between the two main ones. We have assigned this middle ring to CH$_3$ with one quantum in the ν_1 symmetric stretch mode, in correlation with I$(^2P_{3/2})$, as derived from the kinetic energy of the channel. CH$_3(\nu_1=1)$ is visible in this experiment, contrarily to nanosecond experiments, because the *Q* branch of the $3p_z(^2A_2''\leftarrow{}^2A_2'')$ 1_1^1 transition is shifted only 0.4 nm to the red of the $3p_z(^2A_2''\leftarrow{}^2A_2'')$ 0_0^0 transition; that is, well within the bandwidth of the femtosecond probe laser centered at 333.5 nm. Methyl activity in the ν_1 mode had been observed before,[34] mainly—but not solely—in correlation with the I channel, but its detection could not be simultaneous with the *Q* branch of the 0_0^0 transition, since that work was performed with narrow bandwidth, nanosecond lasers.

From angular integration of the images, the CM kinetic energy distributions of CH$_3$ can be extracted for the different pump-probe delay times. The results are shown in Fig. 4, where the three narrow peaks in the distributions correspond to the three resonant processes described above. The sharpness of the peaks is reduced due to the rotational envelope of the probed rotational distribution, with possibly some small contribution coming from vibrationally excited CH$_3$I molecules. The peak corresponding to the CH$_3(\nu=0)+$I$(^2P_{3/2})$ channel has been observed to be systematically broader than that corresponding to the CH$_3(\nu=0)+$I*$(^2P_{1/2})$ peak. This can be attributed to a markedly different degree of rotational excitation for the two channels (see below). Through integration over each peak in the kinetic energy distribution curves, the branching ratio between the I and I* channels (I/I*) in correlation with vibrationless methyl can also be calculated. This ratio has been found to decrease as a function of time from an initial measurable value of 0.16 ± 0.01 at $\Delta\tau$
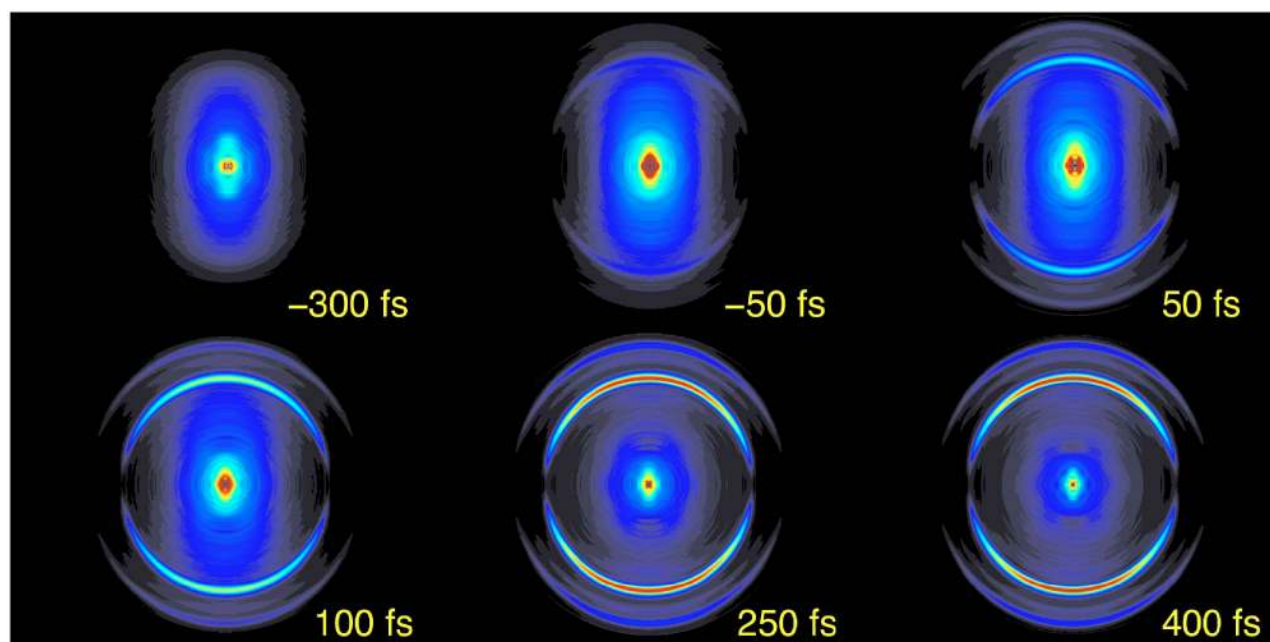
FIG. 3. (Color online) Abel inverted CH_3^+ images obtained upon CH_3I excitation at 266 nm and CH_3 2+1 REMPI at 333.5 nm (Q branch of the $3p_z(^2A_2''$ $\leftarrow ^2A_2'')$ 0_0^0 transition), as a function of pump-probe delay time. The central structure is due to multiphoton ionization processes that are produced by each of the laser pulses separately. Three well-defined rings appear in the image for positive delay times. The inner and outer rings correspond to vibrationless $CH_3(\nu=0)$ formed in correlation with spin-orbit excited $I^*(^2P_{1/2})$ and ground-state $I(^2P_{3/2})$ fragments, respectively. The middle ring corresponds to the channel yielding symmetric stretch mode excited $CH_3(\nu_1=1)$ in correlation with the $I(^2P_{3/2})$ fragments.

=160 fs to an asymptotic value of 0.11 ± 0.02, reflecting the different appearance times of the two channels. The asymptotic value for the ratio is in reasonable agreement with previous data in the literature (0.08 in Ref. 27, 0.064 in Ref. 33, and 0.12 in Refs. 29 and 30).

Radial integration of the images across the radii corresponding to each of the rings yields angular distributions for each channel. For one-photon transitions, we expect an angular dependence of the form $I(\theta)=(\sigma/4\pi)[1$

FIG. 4. (Color online) Center-of-mass kinetic energy distributions of CH_3 upon 266 nm photodissociation of CH_3I and a 2+1 REMPI process of methyl at 333.5 nm, which excites the vibrational components 0_0^0 and 1_1^1 of the $3p_z(^2A_2'' \leftarrow ^2A_2'')$ Rydberg transition. The peaks correspond to the three rings in Fig. 3. Vibrationless methyl is visible, formed in correlation with ground $I(^2P_{3/2})$ and spin-orbit excited $I^*(^2P_{1/2})$ fragments. Methyl with one quantum in the symmetric stretch mode ($\nu_1=1$) formed in correlation with $I(^2P_{3/2})$ is also measurable as an intermediate, weaker peak in the distributions. The results are shown as a function of the pump-probe delay time.

$+\beta P_2(\cos \theta)]$,[61] where σ is the total absorption cross section, θ is the angle between the polarization axis of the photolysis laser and the fragment velocity vector, β is the anisotropy parameter, and $P_2(\cos \theta)$ is the second Legendre polynomial. From least-squares fits to this function, asymptotic values (i.e., for a long pump-probe delay time) obtained for the β parameter are 1.89 ± 0.05, 1.69 ± 0.05, and 1.84 ± 0.08 for the $CH_3(\nu=0)+I^*(^2P_{1/2})$, $CH_3(\nu=0)+I(^2P_{3/2})$, and $CH_3(\nu_1=1)+I(^2P_{3/2})$ channels, respectively. This is in good agreement with previous values reported in the literature. For example, Loo *et al.*[27] give $\beta(I^*)=1.8 \pm 0.1$ and $\beta(I)=1.7 \pm 0.1$. No significant changes in the anisotropy parameter are observed as a function of time well in the asymptotic region. These β values could be affected by fragment alignment effects, but those are very weak for the CH_3 0_0^0 Q branch,[34] as is reflected in our data (only slight differences can be observed in the images when comparing a horizontally versus a vertically polarized probe beam. Note that the images corresponding to a probe beam that is vertically polarized, i.e., perpendicular to the pump beam, are not Abel invertible, since they lack the required cylindrical symmetry).

In order to determine the reaction times of the different channels, integration of each of the resonant peaks in the kinetic energy distribution is performed at each time delay. Figure 5 shows the results obtained for the three channels under study. All channels show a rise that could be adequately fitted with a Boltzmann sigmoidal curve of the form $S \propto \{1+\exp[(t-t_0)/t_C]\}^{-1}$, which is characterized by a center temporal position t_0 (i.e., delay time for which the intensity has reached half its asymptotic value) and a rise time constant t_C, which describes the steepness of the rise. Rise con-
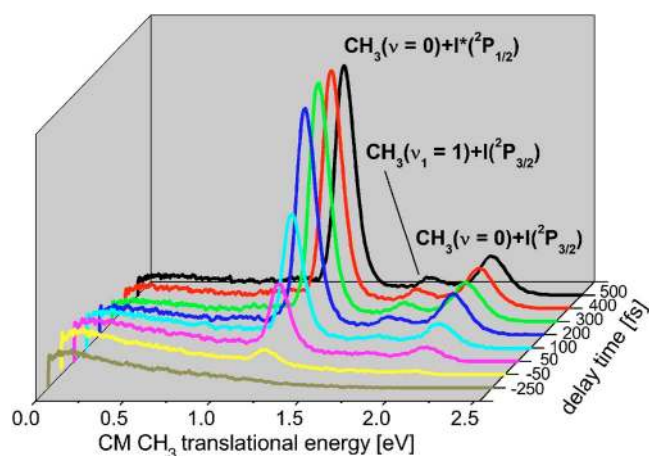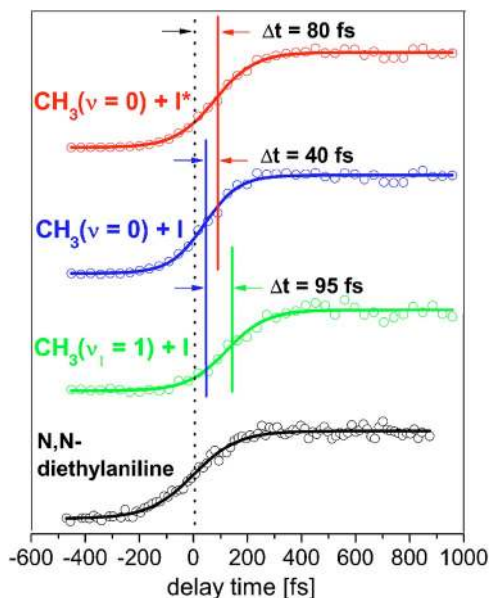
FIG. 5. (Color online) CH$_3$ transients corresponding to the three dissociation channels observed upon 2+1 REMPI at 333.5 nm. (a) CH$_3$(ν=0)+I*($^2P_{1/2}$). (b) CH$_3$(ν=0)+I($^2P_{3/2}$). This gives a measurement of the magnitude of the acceleration of the wave packet motion in the $^1Q_1$ surface compared to the $^3Q_0$ surface. (c) CH$_3$(ν_1=1)+I($^2P_{3/2}$). Note the long delay (95 fs) between the channels producing vibrationless and symmetric stretch excited CH$_3$ in correlation with I($^2P_{3/2}$) fragments (see text). (d) The N,N-diethylaniline parent ion transient measured *in situ* by 1+1′ REMPI sets the time zero for our clock.

stants have been found to be systematically longer for the CH$_3$(ν=0)+I*($^2P_{1/2}$) channel ($t_C^* = 75 \pm 13$ fs) than for the CH$_3$(ν=0)+I($^2P_{3/2}$) channel ($t_C = 64 \pm 7$ fs). Poorer signal-to-noise ratio for the CH$_3$(ν_1=1)+I($^2P_{3/2}$) channel makes the determination of its time constant more uncertain ($t_C^{\nu_1=1} = 73 \pm 22$ fs).

The main result that can be obtained from this work is the temporal delay in the reactions corresponding to each channel. We will define differences in reaction times between the channels as differences in the center temporal position

for their rise curves. They were measured in series of separate experiments and the error bars given correspond to the standard deviation of the set of measurements. As is shown in the figure, the CH$_3$(ν=0)+I*($^2P_{1/2}$) channel is delayed by 40 ± 6 fs with respect to the fastest channel, CH$_3$(ν=0)+I($^2P_{3/2}$). Also, the channel corresponding to symmetric stretch mode excited methyl, CH$_3$(ν_1=1)+I($^2P_{3/2}$), shows a delay of 95 ± 15 fs with respect to its vibrationless counterpart CH$_3$(ν=0)+I($^2P_{3/2}$). The results of this experiment are summarized in Table I.

Absolute determination of reaction delay times with respect to pump-probe laser temporal overlap (zero of time) has been done by an *in situ* measurement of a 1+1′ REMPI signal of the molecule N,N-diethylaniline.[4] The absence of dynamics for this process guarantees that the rise of this signal corresponds to the convolution of a step function at a time defined as the zero of time with the pump-probe cross correlation. Absolute delay time measurements, however, are subject to a greater uncertainty due to the need of using an external reference in an independent experiment. The value thus obtained for the delay time of the main CH$_3$(ν=0)+I*($^2P_{1/2}$) channel with respect to the zero of time is $\Delta\tau_{\text{clocking}} = 80 \pm 20$ fs (see Table I). This value differs slightly with respect to that reported in Ref. 51 (120 ± 30 fs). However, in this case many more experiments have been carried out in order to get better statistics and we consider the present result more accurate.

B. Results on umbrella mode excited CH$_3$(ν_2=1,2)

The appearance of umbrella mode excited methyl was explored by tuning the probe laser to the 2_1^1 and 2_2^2 bands of the $3p_z$($^2A_2'' \leftarrow {}^2A_2''$) transition, via a 2+1 REMPI process at 329.4 and 325.8 nm, respectively.

A sequence of six Abel-inverted images corresponding to the CH$_3^+$ fragment measured for different pump-probe delay times for a probe laser wavelength centered at 329.4 nm [Q branch of the $3p_z$($^2A_2'' \leftarrow {}^2A_2''$) 2_1^1 transition for a two-

TABLE I. Appearance times τ_i, rise times t_C, I/I* branching ratios, and asymptotic anisotropy parameters β, for the different channels of the A-band photodissociation of CH$_3$I observed in this study. Errors are standard deviations of values obtained in typically ten independent experiments.

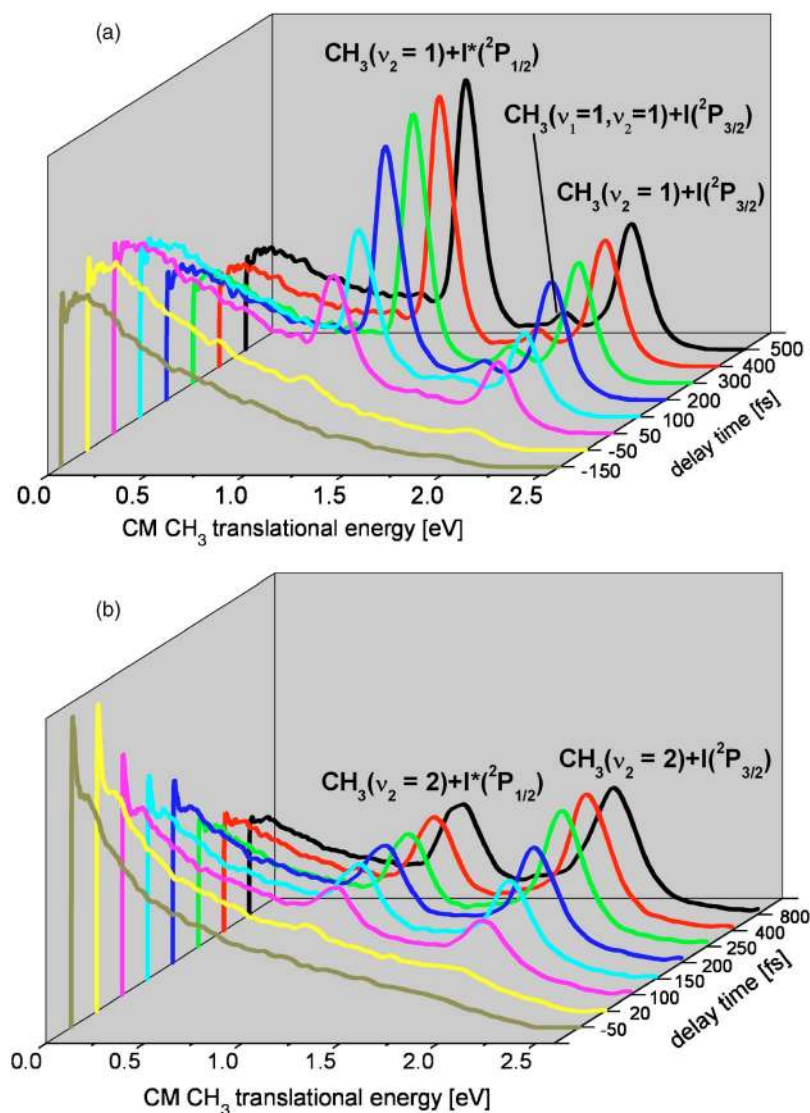| CH$_3$I+$h\nu\rightarrow$	λ_{probe}=333.5 nm	λ_{probe}=329.4 nm	λ_{probe}=325.8 nm
	CH$_3$(ν=0)+I*($^2P_{1/2}$) (1)	CH$_3$(ν_2=1)+I*($^2P_{1/2}$) (1)	CH$_3$(ν_2=2)+I*($^2P_{1/2}$) (1)
	CH$_3$(ν=0)+I($^2P_{3/2}$) (2)	CH$_3$(ν_2=1)+I($^2P_{3/2}$) (2)	CH$_3$(ν_2=2)+I($^2P_{3/2}$) (2)
	CH$_3$(ν_1=1)+I($^2P_{3/2}$) (3)	CH$_3$(ν_1=1,ν_2=1)+I($^2P_{3/2}$) (3)	
τ_1 (fs)	80 ± 20	⋯	⋯
$\tau_1 - \tau_2$ (fs)	40 ± 6	12 ± 10	-28 ± 17
$\tau_3 - \tau_2$ (fs)	95 ± 15	⋯	⋯
$t_C(1)$ (fs)	75 ± 13	66 ± 7	74 ± 16
$t_C(2)$ (fs)	64 ± 7	50 ± 9	64 ± 6
$t_C(3)$ (fs)	73 ± 22	⋯	⋯
I/I* ratio	0.11 ± 0.02	0.45 ± 0.08	1.48 ± 0.21
$\beta(1)$	1.89 ± 0.05	1.97 ± 0.02	1.78 ± 0.03
$\beta(2)$	1.69 ± 0.05	1.97 ± 0.07	1.65 ± 0.03
$\beta(3)$	1.84 ± 0.08	⋯	⋯

FIG. 6. (Color online) Center-of-mass kinetic energy distributions of CH_3 fragments upon 266 nm photodissociation of CH_3I followed by a 2+1 REMPI process of methyl at 329.5 nm, aimed at the excitation of the (a) 2_1^1 and (b) 2_2^2 vibrational components of the $3p_z(^2A_2'' \leftarrow {}^2A_2'')$ Rydberg transition. The two strongest peaks correspond to the two clearly visible rings in the images, where methyl with one quantum in its umbrella mode–$CH_3(\nu_2=1)$–is observed in correlation with spin-orbit excited (inner ring) and ground-state (outer ring) iodine. An additional intermediate ring is also clearly visible in the 2_1^1 case, which can be attributed to methyl excited in both its symmetric stretch and umbrella modes–$CH_3(\nu_1=1,\nu_2=1)$. This transition should therefore correspond to the $1_1^1 2_1^1$ vibrational component of the same transition to the $3p_z$ Rydberg state. The results are shown as a function of the pump-probe delay time.

photon process] can be found in Ref. 62. Similarly to the image sequence for the 0_0^0 band presented above, a structureless background can be seen in the center of the images, corresponding to MPI processes induced by the pump and probe lasers. Again, for sufficiently long pump-probe delay times, three rings appear in the image. The inner and outer rings can be unambiguously assigned to the $CH_3(\nu_2=1)$ $+I^*(^2P_{1/2})$ and $CH_3(\nu_2=1)+I(^2P_{3/2})$ channels. There is an intermediate, much weaker ring, which had not been reported in the literature previously, and that can be assigned to the $CH_3(\nu_1=1,\nu_2=1)+I(^2P_{3/2})$ channel. This assignment is consistent with the available kinetic energy measured from the methyl image. Additionally, the $3p_z(^2A_2'' \leftarrow {}^2A_2'')$ $1_1^1 2_1^1$ combination band transition is shifted only by 0.4 nm to the red of the $3p_z(^2A_2'' \leftarrow {}^2A_2'')$ 2_1^1 transition, that is, well within the bandwidth of the femtosecond probe laser centered at 329.4 nm. Therefore, we believe that this ring corresponds to the formation of methyl excited both in its umbrella and its symmetric stretch modes. Li an Hwang[37] considered the presence of combination $(\nu_1\nu_2)$ bands in their report of CD_3I photodissociation at 266 nm, and in an unpublished high resolution time-of-flight study by Zhu *et al.*,[63] considerable $(\nu_1=1$, all ν_2 states) excitation was observed.

An equivalent temporal sequence of Abel inverted CH_3^+ images where the probe laser has been tuned to 325.8 nm, i.e. the Q branch of the $3p_z(^2A_2'' \leftarrow {}^2A_2'')$ 2_2^2 transition for a two-photon process is provided in Ref. 62. These images show two rings of similar intensities, contrarily to the previous cases, and no evidence for an intermediate combination band ring is present. The inner and outer rings are unambiguously assigned to the $CH_3(\nu_2=2)+I^*(^2P_{1/2})$ and $CH_3(\nu_2=2)+I(^2P_{3/2})$ channels, respectively.

Center-of-mass kinetic energy distributions for the umbrella mode excited methyl fragment are shown in Fig. 6. For the probe laser tuned at 329.4 nm (Q branch of the $3p_z(^2A_2'' \leftarrow {}^2A_2'')$ 2_1^1 transition), shown in Fig. 6(a), the three channels described above can be seen clearly. As had been described previously,[27] the I/I* branching ratio significantly varies for this channel from its vibrationless counterpart, with an asymptotic value of 0.45 ± 0.08. As was the case for the 0_0^0 band, a decrease in the apparent ratio is observed as a function of time, which is related with the difference in reaction times of the two channels (highest observable value was 0.53 ± 0.02, for a delay time of −40 fs). The asymptotic

value for the ratio is somewhat larger than previously reported data (0.30 in Ref. 27, 0.20 in Ref. 33, and 0.37 in Ref. 29).

The analogous experiment performed with a probe laser center wavelength of 325.8 nm [Q branch of the $3p_z(^2A_2'') \leftarrow {}^2A_2'') \, 2_2^2$ transition] yields the kinetic energy distributions shown in Fig. 6(b), where no detectable intermediate peak appears. The asymptotic branching ratio for the I/I* channels has been found to be 1.48 ± 0.21, again larger than previous measurements by other authors [1.1 in Ref. 27 and 0.96 in Ref. 33]. In this case, as will be shown below, the reaction time of the I* channel has been found to be shorter than that of the I channel. Therefore, the apparent I/I* ratio increases as a function of time, contrarily to the 0_0^0 and 2_1^1 bands. The lowest measured value for the ratio is 0.8 ± 0.1, at a delay time of −6 fs.

Asymptotic anisotropy parameters β are 1.97 ± 0.02 for both the I and I* channels in correlation with CH$_3(\nu_2=1)$ and 1.78 ± 0.03 and 1.65 ± 0.03 for the corresponding channels in correlation with CH$_3(\nu_2=2)$. These β parameters do not differ too much from those obtained for the I and I* channels in correlation with CH$_3(\nu=0)$ (see Table I).

Integration of the peaks in the kinetic energy distributions yields the transient signal curves for each channel, from which reaction times can be extracted. These results are shown in Fig. 7, where results for $\lambda_{probe}=329.4$ nm and $\lambda_{probe}=325.8$ nm are presented. In this case, no *in situ* measurement of time zero was made, and as a consequence, only relative timings between channels can be shown. Note how the delay between the CH$_3(\nu_2=1)+I(^2P_{3/2})$ and CH$_3(\nu_2=1)+I*(^2P_{1/2})$ channels $(12 \pm 10$ fs) is significantly reduced compared to its vibrationless counterpart, to the point that, for even higher umbrella mode methyl excitation $(\nu_2=2)$, the I and I* channels appear interchanged in time, the I* preceding the I channel by 28 ± 17 fs. Low signal-to-noise ratio precluded the measurement of the delay time corresponding to the peak ascribed to the CH$_3(\nu_1=1, \nu_2=1)+I(^2P_{3/2})$ channel at 329.4 nm excitation.

Table I summarizes the complete set of measurements performed for the timing of the different channels in the 266 nm CH$_3$I photodissociation. Analysis of the rise curves along the same lines as was described for the previous section (fits with a Boltzmann sigmoidal curve of the form $S \propto \{1+\exp[(t-t_0)/t_C]\}^{-1}$ will give us values for the center temporal position t_0 (i.e., delay time for which the intensity has reached half its asymptotic value) and the rise time constant t_C, related to the steepness of the rise. Rise constants for the 2_1^1 band were found to be shorter than for the 0_0^0 case, and, once again, they are systematically longer for the CH$_3(\nu_2=1)+I*(^2P_{1/2})$ channel $(t_C^*=66 \pm 7$ fs) than for the CH$_3(\nu_2=1)+I(^2P_{3/2})$ channel $(t_C=50 \pm 9$ fs). The same behavior is seen for 2_2^2, where we obtain $t_C^*=74 \pm 16$ fs for the CH$_3(\nu_2=2)+I*(^2P_{1/2})$ channel and $t_C=64 \pm 6$ fs for the CH$_3(\nu_2=2)+I(^2P_{3/2})$ channel.

Figure 8 contains the asymptotic center-of-mass CH$_3$ kinetic energy distributions obtained at all three probe wavelengths used in this study (333.5, 329.4, and 325.8 nm), to-
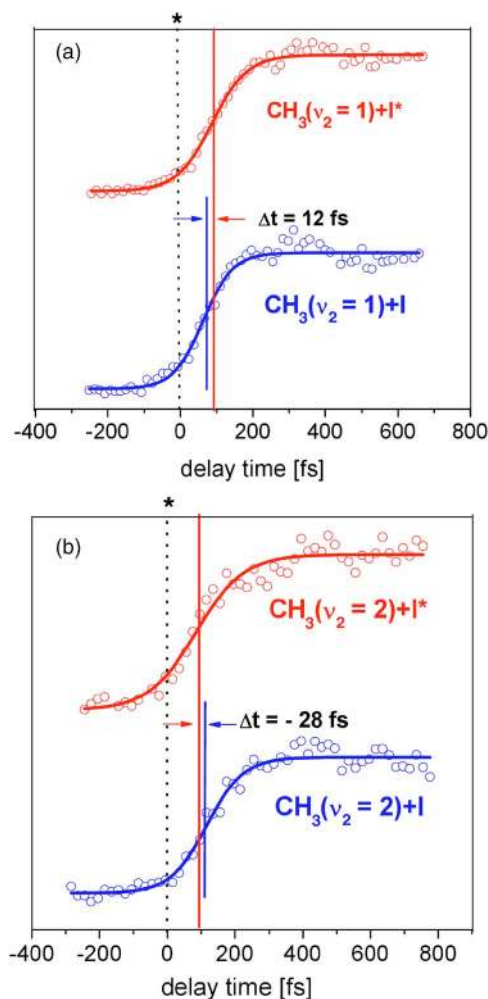

FIG. 7. (Color online) (Top) CH$_3$ transients corresponding to the dissociation channels observed upon 2+1 REMPI at 329.4 nm. (i) CH$_3(\nu_2=1)+I*(^2P_{1/2})$. (ii) CH$_3(\nu_2=1)+I(^2P_{3/2})$. (Bottom) CH$_3$ transients corresponding to the two dissociation channels observed upon 2+1 REMPI at 323.8 nm. (i) CH$_3(\nu_2=2)+I*(^2P_{1/2})$. (ii) CH$_3(\nu_2=2)+I(^2P_{3/2})$. The dashed vertical line indicated with an asterisk represents the zero of time that has been set arbitrarily in both cases to have a time of appearance of the I* channel of 80 fs, which is the clocking time found for the CH$_3(\nu=0)+I*$ channel (see Fig. 5).

gether with the assignments made for all channels. Note that the curves have been normalized to fractional vibrational populations as reported in Ref. 34.

C. Off-resonance measurements

In the previous sections, we have presented results corresponding to 2+1 resonant multiphoton ionization of the methyl fragment resulting from CH$_3$I photodissociation. This method is sensitive to the arrival of the dissociating wave packet to the asymptotic part of the potential energy surface, where resonant absorption occurs, which is why it was used for clocking or "timing" the different reaction channels under observation. However, as was shown in Ref. 64, tuning the probe laser away from the asymptotic resonance can be used to detect transient species. For small detunings, the process can be thought of as that of probing a fragment that is not yet isolated, so that its energy levels are still perturbed by the proximity of the cofragment. For a probe laser that is slightly
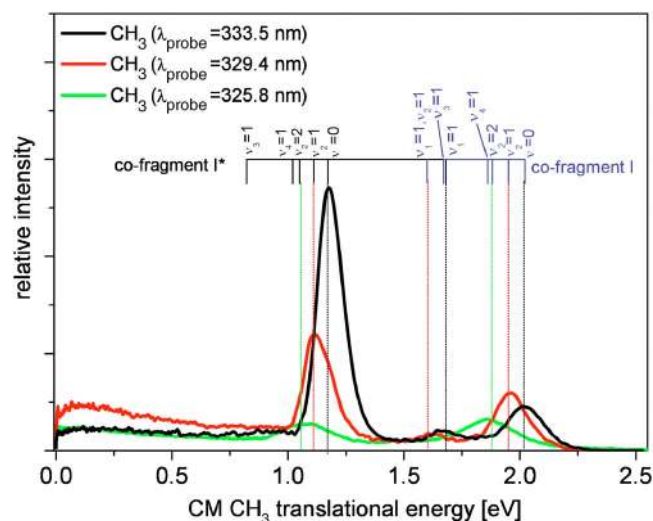
FIG. 8. (Color online) Asymptotic center-of-mass CH_3 kinetic energy distributions obtained at all three probe wavelengths used in this study (333.5, 329.4, and 325.8 nm), together with the assignments made for all channels. Note that the curves have been normalized to fractional vibrational populations as reported in Ref. 34.
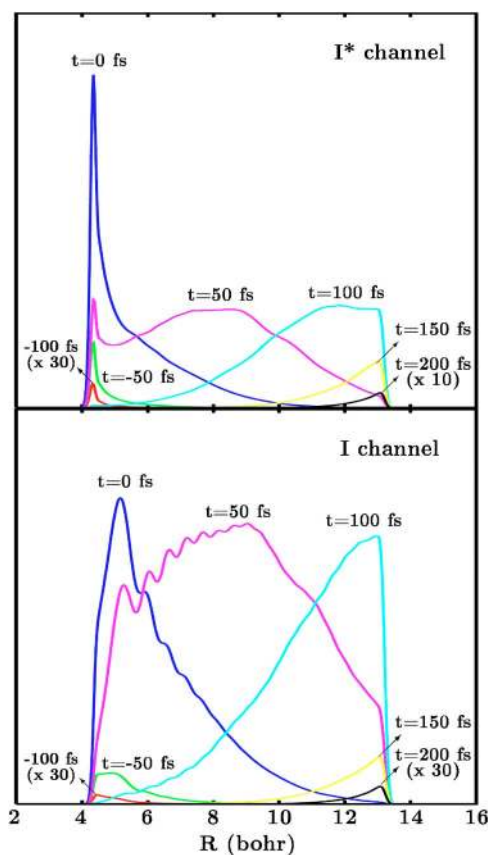

FIG. 9. (Color online) Wave packet distributions in the R coordinate at different times in the $^3Q_0$ (upper panel) and $^1Q_1$ (lower panel) electronic states. Some of the distributions have been multiplied by a factor 10 or 30.

detuned from the resonance of the isolated fragment but in resonance with such a "perturbed" fragment, a fast component is expected as the time delay between the pump and probe lasers is varied, with a maximum corresponding to the time delay corresponding to the resonance of the transient species.

In this work, we have attempted to observe the transient species in CH_3I photodissociation by detuning the probe laser away from the Q branch of the $3p_z(^2A_2'' \leftarrow ^2A_2'')$ 0_0^0 transition at 333.5 nm. Given the spectral proximity of the strong 2_1^1 transition (329.4 nm) and the bandwidth of the femtosecond laser (3 nm), detuning to the blue of the 0_0^0 transition was not possible without observing contamination from the 2_1^1 band. Therefore, only detuning to the red was performed, in steps of 0.5 nm from 333.5 to 336.5 nm. Transient behavior for both the $CH_3(\nu=0)+I^*(^2P_{1/2})$ and the $CH_3(\nu=0)+I(^2P_{3/2})$ channels with the shape of that shown in Fig. 5 was observed in all cases, with decreasing signal intensity as the detuning was larger, but with the absence of a transient, fast component.

It is essential to note that the potential energy surface corresponding to the $CH_3(\nu=0)+I(^2P_{3/2})$ channel is purely dissociative, whereas that corresponding to the $CH_3(\nu=0)+I^*(^2P_{1/2})$ channel presents a shallow well.[32] This means that, as we move from the asymptote towards the bound region, the potential in the $CH_3(\nu=0)+I(^2P_{3/2})$ channel increases monotonously while that of the $CH_3(\nu=0)+I^*(^2P_{1/2})$ channel experiences an initial decrease. As we detune the probe laser from resonance towards the red, we should only expect a transient fast component for the $CH_3(\nu=0)+I(^2P_{3/2})$ channel, while the $CH_3(\nu=0)+I^*(^2P_{1/2})$ channel should only show a decrease in intensity but a conservation of the overall transient shape, as was observed in the experiment. Thus, the question remains as to the absence of a fast component in the $CH_3(\nu=0)+I(^2P_{3/2})$ channel as the detuning to the red is performed. In order to clarify the origin of this behavior, a classical model was used

(see below in the Discussion section). The result of the simulation indicated that the transient feature would have a temporal width of around 10 fs, and would be lost upon convolution with the temporal width of our probe laser, estimated in around 100 fs. The result of the application of the classical model together with a convolution with a Gaussian probe pulse with a realistic temporal width provided transient shapes compatible with those observed in the experiment in all cases.

V. THEORETICAL RESULTS

A. Time-dependent magnitudes

The time evolution of the wave packet in the dissociation coordinate R on the potential surfaces of the $^3Q_0$ and $^1Q_1$ excited electronic states is shown in Fig. 9. The continuously pumping laser pulse creates a wave packet with increasing amplitude in the Franck–Condon region ($3.9a_0 \leqslant R \leqslant 4.2a_0$) of the $^3Q_0$ potential surface. A fraction of the wave packet excited to the $^3Q_0$ surface undergoes a nonadiabatic transition to the $^1Q_1$ electronic state. At relatively short times $t < 50$ fs (the simulation starts at $t_{in}=-150$ fs) most of the wave packet amplitude locates at short distances, where the packets are born on the two potential surfaces.

As time proceeds, the wave packet amplitude originated on both electronic surfaces moves toward the asymptotic region, giving rise to dissociation. Although the excitation pulse is pumping the initial wave packet in the Franck–
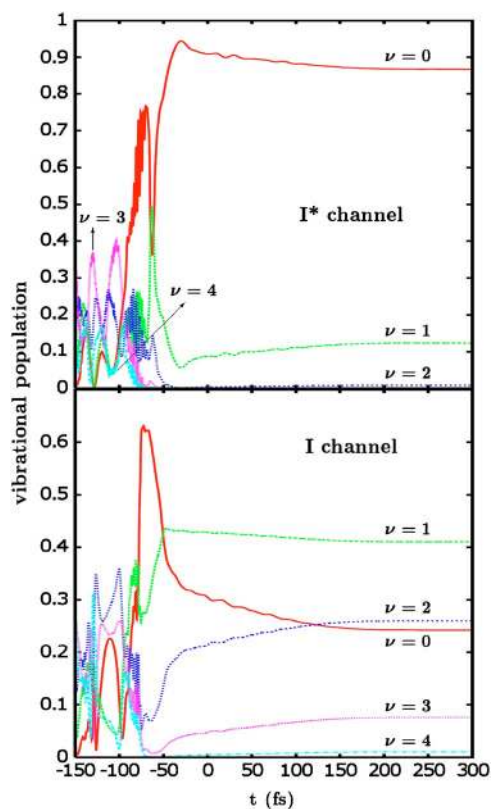
FIG. 10. (Color online) Time evolution of the population $P_\nu^{(i)}(E,t)$ in the five lowest vibrational states of the umbrella mode of the CH$_3(\nu)$ group during dissociation through the I* (upper panel) and the I channels (lower panel). The sum of the vibrational populations in each i dissociation channel is normalized to unity. The $R_c=12.99a_0$ value was used in Eq. (16) to calculate the $P_\nu^{(i)}(E,t)$ populations shown.

FIG. 11. (Color online) Calculated CH$_3$ transients for dissociation of CH$_3$I into CH$_3(\nu=0)+$I*($^2P_{1/2}$) and CH$_3(\nu=0)+$I($^2P_{3/2}$). (a) The transients are computed by fixing $R_c=11.0a_0$ in Eq. (16). (b) Each transient shown is an average of several transient curves calculated for different values of R_c in Eq. (16) (see the text for details). In both panels the I channel transient has been rescaled in order to match the same height as the I* channel transient for long times.

Condon region from $t=-150$ to $t=150$ fs, the wave packet amplitude at large distances becomes dominant for times $t>50$. The wave packet is absorbed in the region $R>13.0a_0$, and at $t\sim200$ fs all the wave packet has been absorbed in practice. The wave packet develops some small undulations, more conspicuous in the amplitude undergoing a nonadiabatic transition (the I channel) and in the interaction region. Such undulations are probably the result of interference between wave packet amplitude populating different internal states of the CH$_3$ group along the dissociation process.

Analysis of the time evolution of the population in the vibrational states of the CH$_3$ umbrella mode provides some insight on how the CH$_3$I dissociation takes place (in what follows we will refer to ν as the vibrational quantum number of the umbrella mode of the CH$_3$ fragment within the pseudotriatomic model employed to describe the CH$_3$I system; thus, $\nu=1,2$ would be equivalent to $\nu_2=1,2$). Such evolution is displayed in Fig. 10 for the two dissociation channels. The population curves show a remarkably oscillating behavior until nearly $t=-30$ fs, and then they gradually stabilize at their final asymptotic values. A similar behavior of the time-dependent vibrational populations of the product fragment has been found in the vibrational predissociation of van der waals clusters such as Cl$_2$–He$_2$.[65] The oscillations in the curves of Fig. 10 indicate rapid transfer of population between the CH$_3$ vibrational states populated in each dissociation channel. In this sense we note that superimposed on
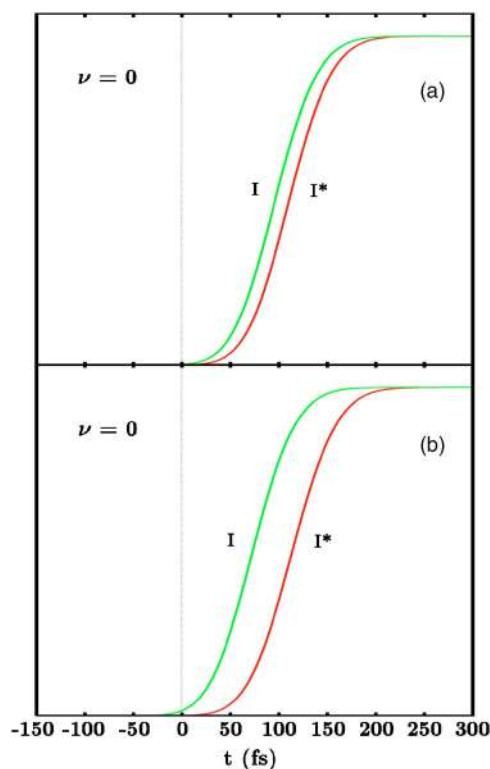
some of the bigger oscillations there appears a set of smaller, faster oscillations (like those displayed in all the population curves of the I* channel in the range between $t\sim-100$ and $t\sim-70$ fs). The exchange of vibrational population found in the curves reveals a strong coupling between the vibrational states of CH$_3$ in the CH$_3$–I interaction region.

One of the central quantities measured experimentally is the time-dependent transient signal of appearance of CH$_3$ +I*(I) products. Transient curves $P_\nu^{(i)}(E,t)$ associated with CH$_3$I dissociation into CH$_3(\nu=0)+$I*($^2P_{1/2}$) and CH$_3(\nu=0)$ +I($^2P_{3/2}$) for 266 nm excitation have been calculated fixing $R_c=11.0a_0$ in Eq. (16), and they are shown in Fig. 11(a). We consider that at this value of R_c the interaction between the two fragments is negligible. The time associated with half the asymptotic value of each calculated transient curve gives the theoretical dissociation reaction time or appearance time τ corresponding to each dissociation channel. The appearance times obtained from the transients of Fig. 11(a) are τ_1 =110.6 and τ_2=96.1 fs for the I* and I channels, respectively. The calculated absolute appearance time τ_1 is in agreement with the appearance time $\tau_1=80\pm20$ fs found experimentally for dissociation into CH$_3(\nu=0)+$I*($^2P_{1/2}$) at 266 nm. However, the relative appearance time obtained from the simulation, $\tau_1-\tau_2=14.5$ fs, appears to be too short in comparison to the experimental relative appearance time for these dissociation channels, $\tau_1-\tau_2=40\pm6$ fs.
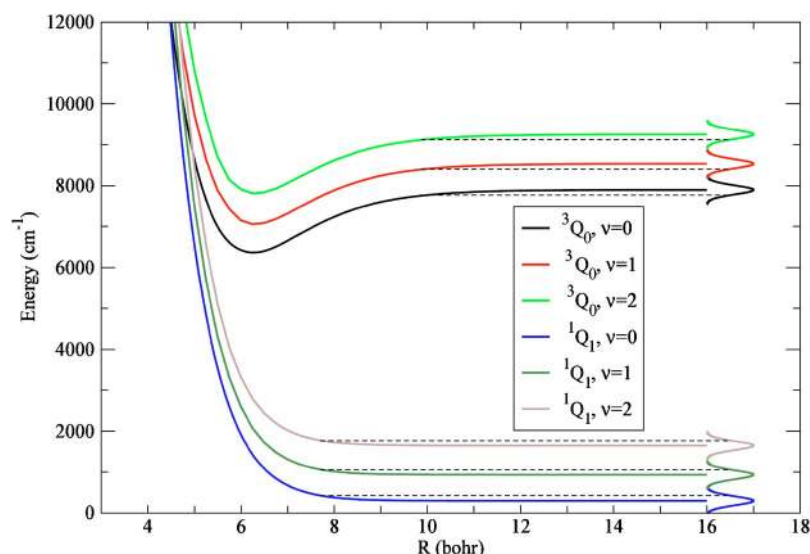
FIG. 12. (Color online) Adiabatic potential energy curves associated with the $^3Q_0$ and $^1Q_1$ electronic states of $CH_3(\nu)-I$ vs R for the first three vibrational states ν of CH_3. The energy dispersion distributions of the probe laser pulse are also shown in the figure. The dashed lines indicate the R distances for which the potential curves reach the value of 129 cm^{-1} above or below the corresponding asymptote, which in turn correspond to the half-maximum point of the (Gaussian) energy dispersion distributions. See the text for details.

The discrepancy between the experimental and the theoretical relative appearance times seems to be very large as to be attributed mainly to the quality of the *ab initio* potential energy surfaces used in the simulations for the $^3Q_0$ and $^1Q_1$ electronic states. There are two additional and probably more important sources for discrepancy in the simulations in comparison with the experiment. One of them is obviously the limitations of the three-dimensional model employed to describe the nine-dimensional CH_3I system. The other possible source of discrepancy is related to the fact that some of the experimental conditions are not realistically considered in the simulation. Since increasing the dimensionality of the model becomes extremely costly, it is on the second source where we can focus in order to improve the quality of our model when compared with experiment.

One of the differences in the conditions of the experiment and the simulation is that the experiment uses a probe laser pulse to excite the fragments in order to detect them, and this probe laser pulse is not considered in the simulation. It is estimated that the spectral energy dispersion of the experimental probe pulse has a half width at half maximum (HWHM) of ~129 cm^{-1} (which corresponds to a FWHM of 2.89 ± 0.13 nm as determined experimentally). This establishes an energy window for the experimental detection of the fragments. In other words, it means that the experiment detects CH_3 and $I^*(I)$ fragments which are not yet completely separated, and which still interact to some extent with an interaction potential energy within the range covered by half the spectral energy dispersion of the probe pulse.[64]

By assuming a Gaussian shape for the probe pulse, the maximum of the energy dispersion distribution of the pulse would correspond to the asymptote of the interaction potential between CH_3 and $I^*(I)$, where the interaction energy of the fragments is nearly zero. The transients of Fig. 11(a), calculated for the large distance $R_c=11.0a_0$, would essentially correspond to the transients detected experimentally near the maximum of the energy dispersion distribution of the probe pulse. However, the experiment detects other transients within the energy window of the dispersion distribution of the probe pulse, which may have different appearance

times. The transient curves obtained experimentally are an average of all the transients detected within the energy window, weighted by the energy dispersion distribution of the probe pulse. This weighted average is missing in the calculated transients of Fig. 11(a) and might be the origin (at least partially) of the discrepancy found.

In order to consider the energy dispersion distribution of the experimental probe pulse in the calculated transient curves, the following strategy was adopted. First, adiabatic potential energy curves in the R coordinate were calculated for the $\nu=0$, 1, and 2 vibrational states of CH_3 in both the $^3Q_0$ and $^1Q_1$ electronic states of CH_3I. This is accomplished by diagonalizing the 3D Hamiltonians $\hat{H}_1$ and $\hat{H}_2$ for the $^3Q_0$ and $^1Q_1$ states at several fixed R distances by means of the FGH method.[58] The eigenvalues of the energy levels $(\nu,j) = (0,0)$, (1, 0), and (2, 0) obtained after diagonalization of $\hat{H}_1$ and $\hat{H}_2$ at each fixed R distance provide the adiabatic potential energy curves for $\nu=0$, 1, and 2 in the $^3Q_0$ and $^1Q_1$ electronic states. Such curves are shown in Fig. 12.

Now the energy dispersion distribution of the experimental probe pulse is modeled as a Gaussian function $G(E)$, with a HWHM of 129 cm^{-1}. This distribution is placed on each adiabatic potential curve such that its maximum coincides with the asymptote of the curve, and therefore its half-maximum point coincides with a potential energy of 129 cm^{-1} relative to the asymptote of each curve, as illustrated in Fig. 12. By doing this one can assign the weight of the energy dispersion distribution $G(E)$ corresponding to a given energy E to a specific R distance on each potential curve, obtaining a weighting distribution in R, $F(R)$. Then, transient curves for the I^* and I dissociation channels in the final states of CH_3 $\nu=0$, 1, and 2 are calculated for 27 different points of R_c in Eq. (16) which cover the relevant range of the $F(R)$ distribution. The calculated transient curves are weighted with the $F(R)$ distribution, and finally an averaged transient curve is obtained for each dissociation channel. The averaged transients corresponding to $\nu=0$ are shown in Fig. 11(b). Similar averaged transients (not shown) are obtained for $\nu=1$ and 2.

TABLE II. Calculated appearance times obtained from the averaged transient curves of Fig. 12 for the I* and I dissociation channels, rise times t_C, and I/I* branching ratios (from Fig. 15) producing CH$_3(\nu)$ fragments in the $\nu=0,1,$ and 2 vibrational states.

	$\nu=0$	$\nu=1$	$\nu=2$
I* channel, τ_1 (fs)	113.8	115.6	118.5
I channel, τ_2 (fs)	72.8	73.7	74.7
$\tau_1 - \tau_2$ (fs)	41.0	41.9	43.8
t_C(I*) (fs)	21.8	21.9	22.0
t_C(I) (fs)	21.0	21.0	21.1
I/I* ratio	0.07	0.76	4.83

The appearance times obtained from the averaged transients are collected in Table II. By comparing the appearance times of Table II for $\nu=0$ with those obtained from the transients of Fig. 11(a), before averaging over the energy dispersion of the probe pulse, significant changes are found. The time τ_1 does not change much, only increasing slightly from 110.6 to 113.8 fs. However, τ_2 decreases substantially from 96.1 to 72.8 fs. As a result, the relative appearance time for $\nu=0$ now becomes $\tau_1-\tau_2=41.0$ fs, in very good agreement with the experimental result of 40 ± 6 fs. It therefore appears that including in the simulation the spectral energy dispersion of the experimental probe laser pulse has an important effect on the results, in particular for the I dissociation channel.

The appearance times for $\nu=1$ and 2 (both the absolute and the relative ones) just increase slightly in comparison with those of $\nu=0$. These small increases are related to the fact that, as the vibrational state of CH$_3$ is excited there is somewhat less energy available for the recoiling fragments, and dissociation becomes somewhat slower. The appearance times obtained from the simulation suggest no significant differences between the dissociation mechanisms producing CH$_3$ fragments in the $\nu=0$, 1, and 2 vibrational states, at variance with the observations, which predict a substantial decrease, and even inversion, of the relative time of the I and I* channels as vibrational excitation in the CH$_3$ umbrella mode increases (see Table I).

We have fitted the average transients for $\nu=0$, $\nu=1$, and $\nu=2$ to the same Boltzmann sigmoidal curve as in the experimental case. The values of t_C found for the different transients are listed in Table II. The t_C values obtained theoretically follow the same trend found experimentally for all vibrational states of the CH$_3$ fragment; i.e., the I* transients have a slightly slower rise than the I transients. However, the differences in the theoretical case are substantially smaller than in the experiment.

B. Product fragment state distributions

The present simulations of the CH$_3$I photodissociation dynamics use for the first time the recently reported *ab initio* potential[47] for the C-I interaction in the ground electronic state. It is thus interesting to analyze the fragment vibrational and rotational distributions currently obtained and to com-
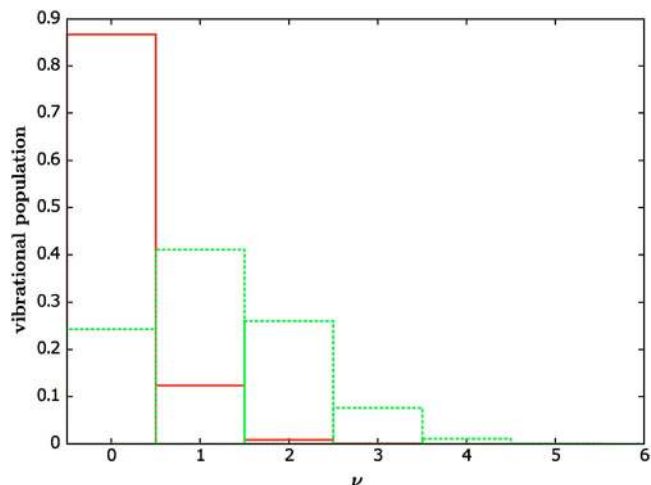

FIG. 13. (Color online) Calculated vibrational distributions of the CH$_3(\nu)$ fragment produced through the I* (solid boxes) and the I channels (dashed boxes).

pare them to previously calculated distributions in order to assess the effect of the new potential.

Rovibrational state distributions $P_{\nu,j}^{(i)}(E,t)$ of the CH$_3$ fragment were calculated with Eq. (16) and E corresponding to excitation with 266 nm radiation for the asymptotic value $R_c=12.99a_0$ for the I* and I dissociation channels ($i=1,2$). In these calculations the wave packet was projected out onto fragment states up to $\nu=6$ and $j=23$. Asymptotic rovibrational distributions $P_{\nu,j}^{(i)}(E,t_{\text{fin}})$ were obtained at final time of the propagation. Asymptotic vibrational distributions are then obtained as

$$P_{\nu}^{(i)}(E,t_{\text{fin}}) = \sum_j P_{\nu,j}^{(i)}(E,t_{\text{fin}}).$$

Vibrational distributions of the CH$_3$ fragment are presented in Fig. 13 for the I* and I dissociation channels. The I* channel distribution is quite cold, with most of the population in the ground vibrational state $\nu=0$. The I channel distribution is significantly hotter, with a maximum at $\nu=1$. As previously discussed,[35,44] the shape of the I* channel vibrational distribution is determined by the fact that the equilibrium geometry of the $^3Q_0$ state corresponds to r distances close to the ground-state equilibrium geometry in the Franck–Condon region. This causes the $\nu=0$ state of CH$_3$ to be the most populated one upon excitation of CH$_3$I to the $^3Q_0$ state. During dissociation in the $^3Q_0$ state, the initial pyramidal structure of CH$_3$ within CH$_3$I changes smoothly to a planar structure of the CH$_3$ fragment. This smooth geometrical change prevents significant vibrational excitation and produces a cold distribution. On the contrary, the equilibrium geometry in the r coordinate in the $^1Q_1$ state is rather different from the r equilibrium geometry in the $\widetilde{X}$ state. Therefore, the geometry change undergone by CH$_3$ upon the CH$_3$I nonadiabatic transition to $^1Q_1$ is larger, involving a higher vibrational excitation of the CH$_3$ fragment produced through the I dissociation channel. On the contrary, the equilibrium geometry in the r coordinate in the $^1Q_1$ state is rather different from the r equilibrium geometry in the $^3Q_0$ state. Indeed, in the conical intersection region the CH$_3$ geometry

is pyramidal in the $^3Q_0$ state while it is nearly planar in the $^1Q_1$ state.[32] Therefore, the geometry change undergone by CH_3 upon the CH_3I nonadiabatic transition from $^3Q_0$ to $^1Q_1$ is larger, involving a higher vibrational excitation of the CH_3 fragment produced through the I dissociation channel.

The present vibrational distributions can be compared to those reported in Ref. 35 (using the same excited electronic potential surfaces and nonadiabatic coupling and a similar dynamical model) for the initial ground state $|J_i M_i K_i\rangle = |000\rangle$ of CH_3I, assuming excitation with 266 nm only through a parallel transition to the $^3Q_0$ state as in the current work. Agreement is found to be very good. Indeed, the vibrational populations reported for the I* channel in Ref. 35 for $\nu=0$, 1, and 2 are 0.84, 0.15, and 0.01, while our corresponding populations are 0.87, 0.12, and 0.01, respectively. Similarly, for the I dissociation channel, the $\nu=0$, 1, 2, 3, and 4 populations found in Ref. 35 are 0.24, 0.39, 0.26, 0.09, and 0.02, while in our case the corresponding populations are 0.24, 0.41, 0.26, 0.08, and 0.01, respectively. The small differences can be attributed to the somewhat different initial state of the two simulations and the fact that the treatment of Ref. 35 includes nonzero total angular momentum effects. Our vibrational distributions agree well with the experimental ones,[34] although they are colder for both dissociation channels.

The distributions of Fig. 13 are also in good agreement with those reported by Guo for 266 nm (see Fig. 3 of Ref. 44). However, the agreement is somewhat worse than that found with the distributions of Ref. 35, particularly in the case of the I* channel distribution, which is produced appreciably colder in the present calculation. This result is not surprising because, in addition to differences in the initial state and transition dipole moment function, the six-dimensional excited electronic potential surfaces of Amatatsu *et al.*[43] were used in Ref. 44.

Rotational distributions of CH_3 produced through the I* and I dissociation channels for the first three vibrational states are shown in Fig. 14. The I* channel rotational distributions are relatively cold, with peaks at $j=1$ (for $\nu=0$) and at $j=2$ (for $\nu=1,2$). The I channel distributions are appreciably hotter than those of the I* channel, peaking at $j=3$ for the three vibrational states and populating a wider range of rotational states. For both dissociation channels the rotational distributions corresponding to the three vibrational states of CH_3 are quite similar. The distributions of Fig. 14 are again quite similar to the vibrational state averaged rotational distributions reported in Ref. 35 for $J=0$ and for the $|J_i M_i K_i\rangle = |000\rangle$ initial state of CH_3I. Good agreement is also found with the distributions reported in Ref. 44 (see Fig. 8 of that work), although the differences here are larger than with the distributions of Ref. 35, as found in the case of the vibrational distributions.

The yield of I* product fragments upon photodissociation of CH_3I for 266 nm excitation has been computed as the sum of the asymptotic rovibrational state populations in the $^3Q_0$ state, divided by the total asymptotic population in both the $^3Q_0$ and $^1Q_1$ states. The result found is that 87.9% of the
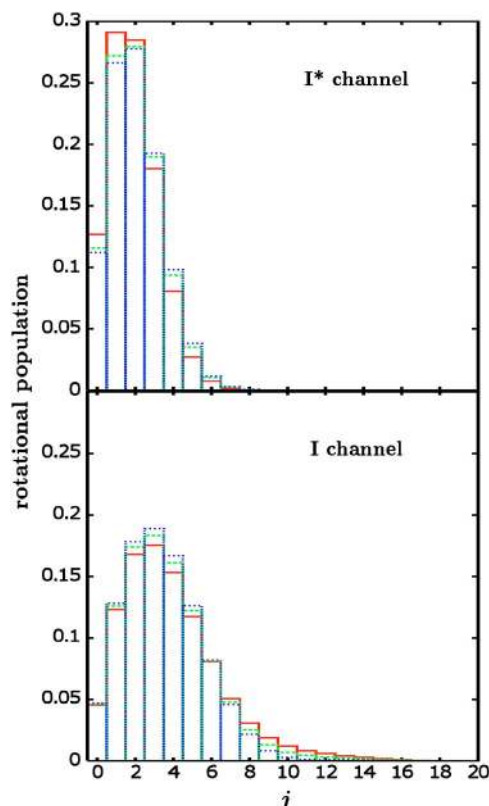

FIG. 14. (Color online) Calculated rotational distributions of the $CH_3(\nu)$ fragment produced through the I* (upper panel) and the I channels (lower panel) for the first three vibrational states $\nu=0$ (solid boxes), $\nu=1$ (dashed boxes), and $\nu=2$ (dotted boxes).

CH_3I dissociation occurs through the I* channel. This yield agrees well with the results of 86% and 89% reported in Refs. 35 and 44, respectively, for 266 nm.

Asymptotic translational energy distributions of the $CH_3(\nu)$ fragments produced upon photodissociation with 266 nm are shown in Fig. 15 for $\nu=0$, 1, and 2. These distributions were obtained with the same averaging procedure
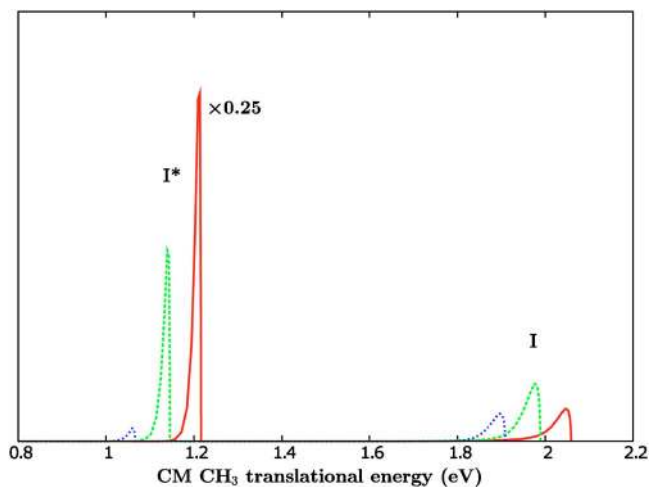

FIG. 15. (Color online) Calculated averaged translational energy distributions of the $CH_3(\nu)+I*(I)$ fragments produced upon photodissociation with 266 nm radiation for the first three vibrational states $\nu=0$ (solid line), $\nu=1$ (long-dashed line), and $\nu=2$ (short-dashed line) vs the translational energy of the CH_3 center of mass. The peak associated with the $CH_3(\nu=0)+I*(^2P_{1/2})$ fragments is multiplied by a factor 0.25.

used to calculate the averaged transient curves of Fig. 11(b), which was already discussed above. The distributions consist of two peaks associated with the I* and I dissociation channels and separated by the spin-orbit splitting between the I*($^2P_{1/2}$) and I($^2P_{3/2}$) electronic states. As the vibrational state of CH₃ becomes excited, the position of the peaks shifts towards lower translational energies, as a consequence that the energy available for the fragments decreases. The peaks associated with the I channel are broader than those of the I* channel, consistently with the larger spreading and excitation of the I channel rotational distributions of Fig. 14. These two facts are in agreement with the asymptotic measured translational energy distributions (see Fig. 8).

Interestingly, Fig. 15 shows that excitation of the CH₃ vibration has a pronounced effect on the relative intensity of the two peaks of the distribution. For $\nu=0$ the I* channel is clearly the dominant one, with the I peak displaying only a small amount of population. However, this situation is gradually inverted as ν increases. Indeed, for $\nu=1$ the intensity of the I channel peak increases substantially, and for $\nu=2$ the I channel already becomes the most likely dissociation channel. This result suggests that, despite the similarities between the appearance times (Table II) and the rotational distributions (Fig. 14) found for different ν final states, still some relevant differences take place in the dissociation process as CH₃ is vibrationally excited. Integration of the peaks for the I and I* channels in the asymptotic translational energy distributions shown in Fig. 15 yields the I/I* ratios shown in Table II. Although the I/I* ratios obtained theoretically increase as vibrational excitation grows, in agreement with experiment, the theoretical values clearly overestimate the experimental ratios, especially for $\nu=2$.

VI. DISCUSSION

One of the most interesting aspects of the photodissociation of CH₃I in the *A* band is the existence of a nonadiabatic crossing between the potential energy curves involved in the reaction: $^3Q_0$ and $^1Q_1$. Since absorption is mainly to the $^3Q_0$ state, which correlates with CH₃ and I*($^2P_{1/2}$) products, the observation of I($^2P_{3/2}$) fragments can only happen through a nonadiabatic process between the two potential surfaces.

In this work, we have been able to experimentally determine reaction times and, particularly, relative times for the different dissociation channels yielding I($^2P_{3/2}$) and I*($^2P_{1/2}$) in correlation with vibrationless or vibrationally excited (in ν_1 or ν_2) CH₃ fragments. As it has been shown in the preceding sections, the channel yielding vibrationless CH₃($\nu=0$) and I($^2P_{3/2}$) is faster by 40 ± 6 fs with respect to that in which I*($^2P_{1/2}$) is produced. This result has been very well accounted for by the wave packet calculation (41 fs) when the appropriate energy window for the detection of the CH₃ fragment, related with the spectral width of the probe laser pulse, is considered. The fact that the I*($^2P_{1/2}$) channel is slower than the I($^2P_{3/2}$) channel in the case of detection of vibrationless CH₃($\nu=0$) can be well understood by considering what fragment is reaching the largest terminal velocity, $v_\infty=(2E/\mu)^{1/2}$, where E is the available energy for the system considering the 266 nm excitation to the $^3Q_0$ potential

surface and the dissociation energy [$D_0=2.42$ eV (Ref. 33)] and μ is the reduced mass. Obviously, the available energy is different for both channels, since the $^3Q_0$ and $^1Q_1$ surfaces differ asymptotically in the amount corresponding to the spin-orbit splitting of the I(^2P) atom, 0.943 eV (see Fig. 1). Thus, the available energy for the I($^2P_{3/2}$) channel will be larger by ≈1 eV than that for the I*($^2P_{1/2}$) channel and the I($^2P_{3/2}$) fragment will reach a larger terminal velocity than the I*($^2P_{1/2}$) fragment.

Using a simple one-dimensional classical model, the dissociation time is given by[66]

$$\tau = \int_{R_i}^{R_f} \frac{dR}{(2[E-V(R)]/\mu)^{1/2}}, \tag{19}$$

where E and $V(R)$ are the available energy and potential energy, respectively, and μ the reduced mass. R_i and R_f are the initial and final distances between the dissociating fragments, respectively. In order to estimate the values of R_f in both $^3Q_0$ and $^1Q_1$ surfaces we consider the spectral width of the probe laser pulse which determines the optical coupling region in the potential energy surface where the free fragments start to be observed experimentally. Considering a HWHM of 129 cm^{-1} for the probe laser pulse, the values of R_f for the I ($^1Q_1$ surface) and I* ($^3Q_0$ surface) channels at which the potential energy reaches 129 cm^{-1} with respect to the asymptote are $7.3a_0$ and $10.1a_0$, respectively. Using these R_f values and the one dimensional $^1Q_1$ and $^3Q_0$ potential energy curves obtained from the Amatatsu *et al.*[32] 9D potential energy surfaces by fixing all coordinates but the C–I distance at the equilibrium configuration, the dissociation times for the I* and I channels are 77 and 42 fs, respectively, the relative time being 35 fs. A similar estimate of the relative time for the two channels from the wave packet calculation using the same R_f values as in the classical model yield a relative time of 36 fs with dissociation times for the I* and I channels of 100 and 64 fs, respectively.

Absolute times have been determined experimentally for the CH₃($\nu=0$)+I*($^2P_{1/2}$), CH₃($\nu=0$)+I($^2P_{3/2}$), and CH₃($\nu_1=1$)+I($^2P_{3/2}$) channels of the reaction by measuring *in situ* the zero of time using the 1+1' REMPI transient of *N,N*-diethylaniline (see Fig. 5). These absolute times are 80 ± 20 and 40 ± 20 fs for the CH₃($\nu=0$)+I*($^2P_{1/2}$) and CH₃($\nu=0$)+I($^2P_{3/2}$) channels and 135 ± 26 fs for the CH₃($\nu_1=1$)+I($^2P_{3/2}$) channel. The theoretical values obtained from the wave packet calculation are 113.8 and 72.8 fs for the CH₃($\nu=0$)+I*($^2P_{1/2}$) and CH₃($\nu=0$)+I($^2P_{3/2}$) channels, respectively. As anticipated before, the observed relative time between these two channels is very well reproduced by the theoretical calculation.

An important result of the present study is the clear change in the relative time between the I and I* channels as CH₃ vibrational excitation in the umbrella mode increases. We have observed that the relative time reduces to 12 ± 10 fs for CH₃($\nu_2=1$) and is even reversed to -28 ± 17 fs for CH₃($\nu_2=2$); i.e., the I* channel is faster than the I channel. This effect is not very intuitive from simple grounds, since the argument employed above to explain the 40 ± 6 fs delay time between the I and I* channels in correlation with

$CH_3(\nu=0)$ in terms of available energies and terminal velocities should be held, in principle, for vibrationally excited $CH_3(\nu_2=1,2)$. It seems, however, that the presence of the nonadiabatic crossing between the $^3Q_0$ and $^1Q_1$ surfaces makes a difference on the timings of the channels where the CH_3 radical is produced with different vibrational energy contents. Our attempts to reproduce this behavior in the wave packet calculations have failed. In the calculations, the absolute and relative times are practically independent of the vibrational excitation of CH_3, as can be seen in Table II. One possible explanation for the failure of the theoretical model is the oversimplification imposed by assuming CH_3I as a pseudotriatomic system. One can argue that some of the couplings between vibrational modes of CH_3I, which are not considered in the wave packet simulation, are important enough as to affect the dynamics of the nonadiabatic crossing towards the different final vibrational states of the CH_3 fragment. Only by considering more degrees of freedom in the theoretical model, would it be possible to understand the role of the couplings between modes on the time-resolved dynamics of the dissociation process. The absolute reaction times obtained theoretically do not change significantly and actually slightly increase when CH_3 appears with more vibrational excitation in the umbrella mode (see Table II). Unfortunately, we have not been able to experimentally determine the absolute times for the channels in which CH_3 appears vibrationally excited in the umbrella mode.

The importance of the couplings between vibrational modes of the CH_3I molecule in the prepared wave packet is also reflected in the theoretical asymptotic I/I* branching ratios. As also evidenced in earlier experiments,[27,34] this ratio changes dramatically in going from vibrationless to vibrationally excited CH_3 (see Table I), indicating that whereas for $CH_3(\nu=0)$ most of the dissociation happens adiabatically through the $^3Q_0$ surface, for $CH_3(\nu_2=1,2)$ nonadiabaticity to the $^1Q_1$ state increases in importance and, particularly for $\nu_2=2$, the yield into the I channel is larger than that into the I* channel. As shown in Table II, the theoretical I/I* ratio increases quite significantly when going from $\nu=0$ to $\nu=1$ and to $\nu=2$. However, while for $\nu=0$ the theoretical and experimental I/I* ratios agree reasonably well, the increase of the theoretical ratios with ν is much larger than the experimentally observed (see Table I). In particular, for $\nu=2$ the experimental I/I* ratio is overestimated by a factor of more than 3. Therefore, the agreement between experimental and theoretical I/I* ratios deteriorates with increasing excitation in the umbrella mode. The theoretical I/I* branching ratios are well affected by the early time dynamics of the wave packet, as it is shown in Fig. 10, where large oscillations of the vibrational populations in both the I and I* channels have been observed before the asymptotic values are reached. These oscillations indicate a very fast transfer of population between the CH_3 vibrational states and are indicative of a strong coupling between the vibrational states of CH_3 in the CH_3-I interaction region. A more realistic model, including more dimensions, would help to understand the role of the couplings between the vibrational modes on the time-resolved multichannel dissociation dynamics.

Another topic for discussion is the long delay found

$(95\pm17 \text{ fs})$ for the channel assigned to $CH_3(\nu_1=1)$ in correlation with $I(^2P_{3/2})$ in comparison with that yielding $CH_3(\nu=0)+I(^2P_{3/2})$. This delay cannot be justified by available energy and terminal velocity considerations since the excess internal energy of $CH_3(\nu_1=1)$ with respect to $CH_3(\nu=0)$ is too small to explain it. Thus, dynamical reasons related with the couplings between modes and the nonadiabatic crossing may be behind this effect. The only previous (indirect) reference to this phenomenon is the work by Johnson *et al.*,[25] where in a frequency domain Raman spectroscopy experiment, they found evidence suggesting that the extension of the C–I bond temporally precedes the onset of the conversion of CH_3 from its tetrahedral configuration to its ultimately planar geometry (umbrella motion) in a few femtoseconds. We have observed this type of behavior directly, but in the CH_3 symmetric stretch motion, with a fundamental frequency of 3004 cm^{-1} versus the 607 cm^{-1} of the umbrella mode. The observed delay time is though somewhat too large in comparison with what is expected. One effect that should be considered is that the detection of the Q branch of the 1^1_1 transition is detuned to the red with respect to the Q branch of the 0^0_0 transition by 0.4 nm. This detuning means that the probing of $CH_3(\nu_1=1)$ occurs at a redder wavelength within the pulse than the probing of $CH_3(\nu=0)$. A simulation based on a simple classical model using the potential energy curves of Amatatsu *et al.* indicates that this detuning would explain a delay between the two channels of a few femtoseconds. This delay could increase if we consider the possibility that the probe pulse has a chirp (something that we cannot prove experimentally). In any case, none of these effects seem to explain such a long delay between the production of $CH_3(\nu=0)$ and $CH_3(\nu_1=1)$ in correlation with $I(^2P_{3/2})$. Thus, as anticipated before, the couplings between modes on the initial wave packet and the nonadiabatic crossing may play a significant role on the time-resolved dynamics of the different vibrational states of the CH_3 product. Only by including more dimensions in the theoretical treatment, the role of the couplings and the nonadiabaticity of the dissociation process could be proven in a reliable manner.

VII. CONCLUSIONS

The combination of femtosecond pump-probe and velocity map ion imaging techniques with resonant multiphoton ionization have allowed the study of the real time photodissociation dynamics of CH_3I from the A band. After electronic excitation with a 266 nm femtosecond laser pulse, the multichannel C–I bond breakage has been followed in time by a delayed femtosecond probe laser, whose wavelength is chosen to ionize different vibrational states of the CH_3 product by 2+1 REMPI. For every vibrational state of CH_3 the two spin-orbit channels producing ground and excited state iodine atoms, $I(^2P_{3/2})$ and $I^*(^2P_{1/2})$, have been resolved in time. We have accurately determined the relative times between the different channels yielding specific vibrational states of the CH_3 fragment. In addition, the absolute reaction times for the channels yielding vibrationless $CH_3(\nu=0)$ have been determined by measuring the zero of time *in situ* using N,N-diethylaniline as reference molecule.

The most relevant experimental results include (a) a decrease in the relative time between the channels producing ground and spin-orbit excited iodine atoms as the vibrational quantum number of the umbrella mode of the CH$_3$ radical increases and (b) a substantial delay time between the channels yielding ground-state iodine atoms in correlation with vibrationless CH$_3(\nu=0)$ and symmetric stretch excited CH$_3(\nu_1=1)$, the latter being slower.

The experimental results have been contrasted to wave packet calculations using a reduced dimensionality (pseudotriatomic) model carried out on the available *ab initio* potential energy surfaces for the CH$_3$I system. Whereas the absolute and relative times of the dissociation channels yielding vibrationless CH$_3(\nu=0)$ fragments are well reproduced by theory, the reduction in relative time between the two iodine channels as vibrational excitation of CH$_3(\nu_2)$ increases is not accounted for by the present theoretical model. It seems that some of the couplings between vibrational modes of CH$_3$I which are not considered in the theoretical wave packet are important enough as to affect the dynamics of the nonadiabatic crossing towards the different final vibrational states of the CH$_3$ fragment. Only by including more degrees of freedom in the theoretical model, would it be possible to understand the role of the couplings between modes on the timeresolved dynamics of the dissociation process. Since the full dimension potential energy surfaces are available for CH$_3$I, the challenge is to extend the wave packet calculations to as many dimensions as possible. Work in that direction is in progress in our group.

ACKNOWLEDGMENTS

[1] A. H. Zewail, Science **242**, 1645 (1988).
[2] A. H. Zewail, Angew. Chem., Int. Ed. **39**, 2586 (2000).
[3] I. V. Hertel and W. Radloff, Rep. Prog. Phys. **69**, 1897 (2006).
[4] D. Zhong and A. H. Zewail, J. Phys. Chem. A **102**, 4031 (1998).
[5] C. Daniel, J. Full, L. González, C. Lupulescu, J. Manz, A. Merli, S. Vajda, and L. Wöste, Science **299**, 536 (2003).
[6] A. M. Rijs, M. H. M. Janssen, E. T. H. Chrysostom, and C. C. Hayden, Phys. Rev. Lett. **92**, 123002 (2004).
[7] O. Gessner, A. M. D. Lee, J. P. Shaffer, H. Reisler, S. V. Levchenko, A. I. Krylov, J. G. Underwood, H. Shi, A. L. L. East, D. M. Wardlaw, E. T. Chrysostom, C. C. Hayden, and A. Stolow, Science **311**, 219 (2006).
[8] B. J. Sussman, D. Townsend, M. Y. Ivanov, and A. Stolow, Science **314**, 278 (2006).
[9] D. Strasser, F. Goulay, and S. R. Leone, J. Chem. Phys. **127**, 184305

(2007).
[10] *Femtochemistry and Femtobiology*, edited by V. Sundström (World Scientific, Singapore, 1998).
[11] S. K. Pal and A. H. Zewail, Chem. Rev. (Washington, D.C.) **104**, 2099 (2004).
[12] D. H. Paik, I. R. Lee, D. S. Yang, J. S. Baskin, and A. H. Zewail, Science **306**, 672 (2004).
[13] I. R. Lee, W. Lee, and A. H. Zewail, Proc. Natl. Acad. Sci. U.S.A. **103**, 258 (2006).
[14] P. Kukura, D. W. McCamant, S. Yoon, D. B. Wandschneider, and R. A. Mathies, Science **310**, 1006 (2005).
[15] T. Baumert, S. Pedersen, and A. H. Zewail, J. Phys. Chem. **97**, 12447 (1993).
[16] B. J. Greenblatt, M. T. Zanni, and D. M. Neumark, Science **276**, 1675 (1997).
[17] A. T. J. B. Eppink and D. H. Parker, Rev. Sci. Instrum. **68**, 3477 (1997).
[18] M. N. R. Ashfold, N. H. Nahler, A. J. Orr-Ewing, O. P. J. Vieuxmaire, R. L. Toomes, T. N. Kitsopoulos, I. A. Garcia, D. A. Chestakov, S. M. Wu, and D. H. Parker, Phys. Chem. Chem. Phys. **8**, 26 (2006).
[19] P. C. Samartzis, B. L. G. Bakker, D. H. Parker, and T. N. Kitsopoulos, J. Phys. Chem. A **103**, 6106 (1999).
[20] W. G. Roeterdink and M. H. M. Janssen, Phys. Chem. Chem. Phys. **4**, 601 (2002).
[21] W. G. Roeterdink, A. M. Rijs, and M. H. M. Janssen, J. Am. Chem. Soc. **128**, 571 (2006).
[22] A. Stolow, A. E. Bragg, and D. M. Neumark, Chem. Rev. (Washington, D.C.) **104**, 1719 (2004).
[23] J. V. V. Kasper and G. C. Pimentel, Appl. Phys. Lett. **5**, 231 (1964).
[24] A. Gedanken and M. D. Rowe, Chem. Phys. Lett. **34**, 39 (1975).
[25] B. R. Johnson, C. Kittrell, P. B. Kelly, and J. L. Kinsey, J. Phys. Chem. **100**, 7743 (1996).
[26] D. W. Chandler and P. L. Houston, J. Chem. Phys. **87**, 1445 (1987).
[27] R. O. Loo, H.-P. Haerri, G. E. Hall, and P. L. Houston, J. Chem. Phys. **90**, 4222 (1989).
[28] I. Powis and J. F. Black, J. Phys. Chem. **93**, 2461 (1989).
[29] D. W. Chandler, J. W. Thoman, Jr., M. H. M. Janssen, and D. H. Parker, Chem. Phys. Lett. **156**, 151 (1989).
[30] D. W. Chandler, M. H. M. Janssen, S. Stolte, R. N. Strickland, J. W. Thoman, and D. H. Parker, J. Phys. Chem. **94**, 4893 (1990).
[31] A. D. Hammerich, U. Manthe, R. Kosloff, H.-D. Meyer, and L. S. Cederbaum, J. Chem. Phys. **101**, 5623 (1994).
[32] Y. Amatatsu, S. Yabushita, and K. Morokuma, J. Chem. Phys. **104**, 9783 (1996).
[33] A. T. J. B. Eppink and D. H. Parker, J. Chem. Phys. **109**, 4758 (1998).
[34] A. T. J. B. Eppink and D. H. Parker, J. Chem. Phys. **110**, 832 (1999).
[35] D. Xie, H. Guo, Y. Amatatsu, and R. Kosloff, J. Phys. Chem. A **104**, 1009 (2000).
[36] A. J. van den Brom, M. L. Lipciuc, and M. H. M. Janssen, Chem. Phys. Lett. **368**, 324 (2003).
[37] G. Li and H. J. Hwang, J. Chem. Phys. **124**, 244306 (2006).
[38] T. F. Hunter and K. S. Kristjansson, Chem. Phys. Lett. **58**, 291 (1978).
[39] R. S. Mulliken, J. Chem. Phys. **8**, 382 (1940).
[40] M. Shapiro and R. Bersohn, J. Chem. Phys. **73**, 3810 (1980).
[41] M. Shapiro, J. Phys. Chem. **90**, 3644 (1986).
[42] H. Guo and G. C. Schatz, J. Chem. Phys. **93**, 393 (1990).
[43] Y. Amatatsu, K. Morokuma, and S. Yabushita, J. Chem. Phys. **94**, 4858 (1991).
[44] H. Guo, J. Chem. Phys. **96**, 6629 (1992).
[45] M.-Y. Zhao, Q.-T. Meng, T.-X. Xie, K.-L. Han, and G.-Z. He, Int. J. Quantum Chem. **101**, 153 (2005).
[46] D. Ajitha, M. Wierzbowska, R. Lindh, and P. A. Malmqvist, J. Chem. Phys. **121**, 5761 (2004).
[47] A. B. Alekseyev, H.-P. Liebermann, R. J. Buenker, and S. N. Yurchenko, J. Chem. Phys. **126**, 234102 (2007).
[48] A. B. Alekseyev, H.-P. Liebermann, and R. J. Buenker, J. Chem. Phys. **126**, 234103 (2007).
[49] M. H. M. Janssen, M. Dantus, H. Guo, and A. H. Zewail, Chem. Phys. Lett. **214**, 281 (1993).
[50] J. C. Owrutsky and A. P. Baronavski, Chem. Phys. Lett. **222**, 335 (1994).
[51] R. de Nalda, J. G. Izquierdo, J. Durá, and L. Bañares, J. Chem. Phys. **126**, 021101 (2007).
[52] Our design is based on the original design by Prof. D. Gerlich (http://www.tu-chemnitz.de/physik/ION/Technology/Piezo-Valve/index.html).
[53] G. A. Garcia, L. Nahon, and I. Powis, Rev. Sci. Instrum. **75**, 4989

(2004).

[54] H. Guo, Chem. Phys. Lett. **187**, 360 (1991).

[55] H. Guo, K. Q. Lao, G. C. Schatz, and A. D. Hammerich, J. Chem. Phys. **94**, 6562 (1991).

[56] E. J. Heller, J. Chem. Phys. **68**, 3891 (1978).

[57] C. C. Marston and G. G. Balint-Kurti, J. Chem. Phys. **91**, 3571 (1989).

[58] H. Tal-Ezer and R. Kosloff, J. Chem. Phys. **81**, 3967 (1984).

[59] G. G. Balint-Kurti, R. N. Dixon, and C. C. Marston, J. Chem. Soc., Faraday Trans. **86**, 1741 (1990).

[60] G. G. Balint-Kurti, R. N. Dixon, and C. C. Marston, Int. Rev. Phys. Chem. **11**, 317 (1992).

[61] R. N. Zare, *Angular Momentum: Understanding Spatial Aspects in*

Chemistry and Physics (Wiley, New York, 1998).

[62] See EPAPS Document No. E-JCPSA6-129-611825 for color figures showing ion images taken at different delay times between the pump and probe femtosecond laser pulse. For more information on EPAPS, see http://www.aip.org/pubservs/epaps.html.

[63] See Ref. 15 in Ref. 34.

[64] M. J. Rosker, M. Dantus, and A. H. Zewail, J. Chem. Phys. **89**, 6113 (1988).

[65] A. García-Vela, J. Chem. Phys. **122**, 014312 (2005); **122**, 216101 (2005).

[66] Q. Liu and A. H. Zewail, J. Phys. Chem. **97**, 2209 (1993).